Journal Pre-proofs

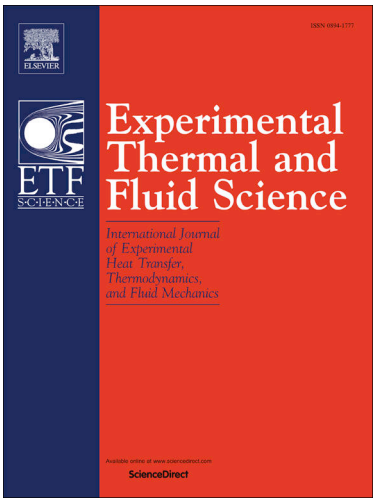

Study of ramp-induced turbulent boundary layer separation and reattachment via temperature-sensitive paint and Lagrangian particle tracking

Marco Costantini, Christian Klein, Andrea De Vincenzo, Reinhard Geisler, Philipp Godbersen, Jonathan Lemarechal, Daniel Schanz, Andreas Schröder, Tobias Knopp, Cornelia Grabe, Stephan Sattler, Massimo Miozzi

PII: S0894-1777(26)00134-2
DOI: https://doi.org/10.1016/j.expthermflusci.2026.111822
Reference: ETF 111822

To appear in: *Experimental Thermal and Fluid Science*

Received Date: 31 January 2026
Revised Date: 29 May 2026
Accepted Date: 14 August 2026

Please cite this article as: M. Costantini, C. Klein, A.D. Vincenzo, R. Geisler, P. Godbersen, J. Lemarechal, D. Schanz, A. Schröder, T. Knopp, C. Grabe, S. Sattler, M. Miozzi, Study of ramp-induced turbulent boundary layer separation and reattachment via temperature-sensitive paint and Lagrangian particle tracking, *Experimental Thermal and Fluid Science* (2026), doi: https://doi.org/10.1016/j.expthermflusci.2026.111822

This is a PDF of an article that has undergone enhancements after acceptance, such as the addition of a cover page and metadata, and formatting for readability. This version will undergo additional copyediting, typesetting and review before it is published in its final form. As such, this version is no longer the Accepted Manuscript, but it is not yet the definitive Version of Record; we are providing this early version to give early visibility of the article. Please note that Elsevier's sharing policy for the Published Journal Article applies to this version, see: https://www.elsevier.com/about/policies-and-standards/sharing#4-published-journal-article. Please also note that, during the production process, errors may be discovered which could affect the content, and all legal disclaimers that apply to the journal pertain.

© 2026 The Author(s). Published by Elsevier Inc.

Journal Pre-proofs

Submitted to the Special Issue of *Experimental Thermal and Fluid Science* (*ETFS*) dedicated to the 6th International Conference on Experimental Fluid Mechanics (ICEFM). Revision R1

Study of Ramp-Induced Turbulent Boundary Layer Separation and Reattachment via Temperature-Sensitive Paint and Lagrangian Particle Tracking

Marco Costantini[a*], Christian Klein[a], Andrea De Vincenzo[a,b], Reinhard Geisler[a], Philipp Godbersen[a], Jonathan Lemarechal[a], Daniel Schanz[a], Andreas Schröder[a,c], Tobias Knopp[a], Cornelia Grabe[a], Stephan Sattler[d], Massimo Miozzi[e]

[a] DLR, Institute of Aerodynamics and Flow Technology, Bunsenstrasse 10, D-37073 Göttingen, Germany

[b] Politecnico di Milano, School of Industrial and Information Engineering, Via La Masa 34, I-20156 Milan, Italy

[c] Brandenburg TU, Chair of Image Based Measurement Techniques, Platz der Deutschen Einheit 1,

D-03046 Cottbus, Germany

[d] TU Braunschweig, Institute of Fluid Mechanics, Hermann-Blenk-Str. 37, D-38108 Braunschweig, Germany

[e] CNR, Institute of Marine Engineering, via di Vallerano 139, I-00128 Rome, Italy

*Marco.Costantini@dlr.de

Journal Pre-proofs

Abstract

An extensive experimental investigation of geometry-induced flow separation and reattachment of a turbulent boundary layer at nearly-zero pressure gradient was conducted in the Large Water Tunnel Braunschweig on a flat-plate configuration featuring a 25° backward-facing ramp. The examined ramp Reynolds number, based on the freestream velocity and on the ramp height, was 8,800. Lagrangian particle tracks and surface temperature maps were highly resolved in space and time via 3D Shake-The-Box and temperature-sensitive paint, respectively, whereas the time-averaged surface pressure distribution was measured by means of pressure taps. This enabled a description of the evolution of the attached boundary layer approaching the ramp, of the shear layer, of the recirculation zone, of flow reattachment, and of the recovery region further downstream. The time-averaged map of the celerity of propagation of temperature fluctuations was determined via analysis of the time-resolved surface temperature maps, while time- and spanwise-averaged distributions of flow velocity, acceleration and Reynolds stresses were obtained via bin-averaging of the Lagrangian particle tracks. The distributions of temperature fluctuation celerity and flow velocity allowed the identification of the time-averaged reattachment location, which was found to be in mutual, reasonable agreement for the two different methods, and also in agreement with previous work on 25° backward-facing ramps. Furthermore, the instantaneous flowfield and surface temperature data enabled capturing the arrangement and evolution of the turbulent flow structures and of their wall thermal traces in the aforementioned flow regions. Spectral analysis of the fluctuating wall temperature and velocity fields showed consistent evolution of these flow features; in particular, in the attached flow regions populated by

streamwise-oriented structures, reasonable agreement was found for the spanwise wavenumbers corresponding to the maxima of the respective power spectra.

Keywords

Turbulent Boundary Layer, Separation, Reattachment, Temperature-Sensitive Paint, Lagrangian Particle Tracking, Shake-The-Box, Celerity of Propagation

1 Introduction

The understanding and prediction of turbulent separated flows are crucial in a variety of aerodynamic and hydrodynamic applications [1,2]. Striking examples are the impact of turbulent flow separation on the aerodynamic performance of wind-turbine rotor blades [3] and transport aircraft wings at the borders of the flight envelope (e.g., at low-speed/high-lift conditions) [4]. Flow scenarios in which the separated, turbulent shear layer reattaches to the surface, thus forming a Turbulent Separation Bubble (TSB), are of particular relevance in practical engineering configurations [5,6]. However, they are still challenging to be predicted for the following reasons: the number of flow parameters influencing the TSB shape, size, and behavior (boundary-layer thickness at separation, Mach number, freestream turbulence, pressure gradient, aspect ratio of the flow apparatus, among others) [5]; the three-dimensional nature of flow separation and reattachment even in a statistically two-dimensional flow [7,8]; and the unsteady phenomena with a broad range of temporal scales characteristic of TSBs [7,9–11]. Reference two-dimensional configurations for the study of TSBs in incompressible flows are the Backward-Facing Step (BFS) [5–6,9,12–18], Backward-Facing Ramps (BFRs) [19–30], and two-dimensional humps [7–8,31–32], whereas the three-dimensional hump discussed in, e.g., [33] is an example of reference three-dimensional configuration.

Focusing on two-dimensional configurations, the BFS flow has been considered in several investigations (see, e.g., [5–6,9,12–18]) because of its practical relevance and the involvement of the crucial features of separated flows, in spite of its simple geometry. Increased complexity to the understanding and prediction of the flow evolution is already added by a relatively small change in the geometry: from BFS to BFR [19–30]. Depending on the ramp geometry and on the aforementioned flow parameters, flow separation can occur directly at the ramp edge (*geometry-induced* TSB) or further downstream (*pressure-induced* TSB) [26,28,34]. The further increase in geometrical complexity represented by a two-dimensional hump (see, e.g., [7,31]) has led to particular challenges in the TSB prediction, as summarized in [35]. Simulations based on the Reynolds-Averaged Navier-Stokes (RANS) equations, which are currently standard for the aerodynamics/hydrodynamics prediction in a variety of applications, failed in the prediction of the TSB induced by the two-dimensional hump (in particular of the reattachment location), although the used turbulence models were capable to predict correctly the extent of the TSB for the aforementioned BFS flow [35], thus leading to contradictive results. Even in most recent publications (as, for instance, in [8]), current modeling approaches are reported to “have significant difficulty in accurately predicting turbulent separated flows relevant to off-design aerodynamic conditions”. Accordingly, further research is required to improve the understanding of the flow evolution even for reference flow configurations, and thus also

enabling an advancement in turbulence modeling. To pursue these objectives, "high-quality, detailed benchmark experimental data sets" are strongly needed [8].

Various measurement techniques have been used to study TSBs in reference flow configurations, in particular: steady [7–8,10–11,14,22–26,28,32,36–38] and unsteady pressure sensors [7–8,10–11]; hot-wire [24–25,36,38] and hot-film anemometry [37]; thermal tufts [14] and calorimetric sensors based on micro-electro-mechanical systems [10–11,26,28,30]; laser-Doppler velocimetry [13–14,19,23,36,38] and Particle Image Velocimetry (PIV) [7–11,17–18,23–26,28,32,37]; oil-flow visualizations [8,10–11,14,22,26,30,38–40] and Oil-Film Interferometry (OFI) [8,14]. Although this list and the provided references are not meant to be exhaustive, they indicate that – even in recent studies – experimental data in the flowfield were mainly measured in profiles and planes, except for the measurements via volumetric particle tracking velocimetry reported in [39]. In that latter experiment, however, the particle concentration was low, with a mean particle distance corresponding to approx. 1/5 of the (rounded) ramp heigh h. Furthermore, quantitative information on the surface was obtained only at discrete locations; this holds also for the OFI measurements, since the oil was applied in patches [8,14]. For these reasons, additional efforts were necessary to capture three-dimensional phenomena characteristic of TSBs, for example by performing PIV measurements at several planes (see, e.g., [7–8,25]) or by assimilating sparse measurement data via neural networks (as, for example, in [28,30]). Recent developments in Lagrangian Particle Tracking (LPT) [41] by Shake-The-Box (STB) [42–46] and Temperature-Sensitive Paint (TSP) [47–52] have provided methodologies that can enable the measurement of the relevant flowfield and surface information for the experimental study of TSBs without the need of these additional efforts.

The STB technique [42] is a dense three-dimensional LPT method [41] that applies advanced iterative particle reconstruction [44] for the initialization phase and then seizes the temporal information with predictive steps and a local image matching scheme, while extending reconstructed particle trajectories in three dimensions from a few camera projections. In this manner, all components of the velocity and acceleration vectors as well as of the Reynolds stress tensor (including the Reynolds stress anisotropies) can be obtained with high spatial and temporal resolution, while avoiding filtering effects that would reduce the measurement accuracy (as for, e.g., window-correlation based PIV). Furthermore, STB provides a continuous representation of the flowfield, including the streamline curvature. Coupled with the accurate measurement of the Reynolds stresses, this enables a quantification of curvature effects on turbulence enhancement/attenuation.

The TSP technique is based on coatings in which luminescent molecules (the luminophores) are incorporated as sensors [47]. When the luminophores are excited by light in a specific wavelength range, they emit light in a longer wavelength range, the intensity of which decreases at larger temperature. This working principle provides the foundation of the *intensity-based* method for TSP measurements, which enables the non-intrusive measurement of the temperature distribution on the investigated surface (i.e., on the area where the TSP coating has been applied) with high spatial and temporal resolution. More recently, approaches for the identification of flow separation and reattachment as well as for the estimation of the skin-friction field have been proposed [48–52], which rely on time-resolved surface temperature maps measured via TSP. A first application of TSP for the study of a TSB in reference flow configurations has been reported in [40] for a BFS flow in air, showing promising results with regard to the identification of flow reattachment and characteristic TSB modes.

This progress in the STB and TSP techniques and the aforementioned need of high-quality experimental datasets motivated their combination in a new experiment for a reference flow configuration, which was

designed for the study of turbulent separation as well as for the improvement and validation of turbulence modeling. The design and the following experimental activities were conducted within the DLR project *ADaMant* [53]. Among the discussed reference configurations, BFR flows offer an intermediate configuration between the better understood BFS flow and the more challenging hump flows (see above); for this reason, they were selected as the configuration to be examined in this work. As compared to the BFS flow, the influence on a Turbulent Boundary Layer (TBL) of a BFR with sharp edges obviously depends on an additional parameter, i.e., the ramp angle. The effect of the ramp angle on BFR-induced TSBs has been experimentally investigated in a wind tunnel [19] for a range of ramp Reynolds numbers $\mathrm{Re}_h = U_\infty h/\nu = 5{,}000–64{,}000$, where U_∞ is the freestream velocity and ν the kinematic viscosity. In that study, however, the examined aspect ratios of the flow apparatus (also known as Expansion Ratio, ER) were ER = 1.5–3.3, being ER defined as the ratio of the tunnel height H downstream and upstream of the imperfection. (In [19], H was the vertical distance between the investigated surface and the wind-tunnel top wall.) The cases at $\mathrm{Re}_h = 22{,}600$ and ER = 1.5 from that experimental work [19] also served as validation for the numerical study presented in [20], where two different turbulence models used in the RANS simulations provided contradictive results in terms of predicted reattachment location, and both models underpredicted the streamwise velocity fluctuations. An expansion ratio of ER = 1.3, close to those considered in [19], was examined in the wind-tunnel experiments at approx. $\mathrm{Re}_h = 150{,}000$ on a 20° BFR [26,28,30]. Although these ER-values significantly larger than 1 are relevant for internal flows, the expansion ratio should be as close as possible to ER = 1 for achieving a transferability of the results to external, wall-bounded flows, such as the TBL over the wings of commercial transport aircraft. An experimental configuration with a 25° BFR was examined in [23] and [24] at $\mathrm{Re}_h = 92{,}000–246{,}000$ and $\mathrm{Re}_h = 30{,}000–70{,}000$, respectively; the corresponding expansion ratios were ER = 1.1 [23] and 1.064 [24]. The same ramp geometry was considered in the numerical studies of [21,27,29]. RANS simulations were performed at $\mathrm{Re}_h = 123{,}000$ in the first study [21], whereas Large Eddy Simulations (LES) were performed at $\mathrm{Re}_h = 47{,}000$ and 170,000 in [29] and [27], respectively; in all three studies, a slip-wall condition was applied along the top boundary of the investigated configurations. These experimental and numerical investigations focused on sharp-edged, (quasi-) two-dimensional BFRs with 25° ramp angle. (In the experiments, the span width of the BFR was at least 16 h [23,24].) Rounded ramps were studied experimentally in [28,32,36–38] and numerically in [54], among others; a BFR configuration with reduced spanwise extent was examined, e.g., in the experimental work of [22,25,55], where the ratio of BFR span width to height was about 4.

The results of the experimental and numerical investigations on sharp-edged, (quasi-) two-dimensional 25° BFRs [21,23–24,27,29] showed that the TSB comprised only a main recirculation region, i.e., without secondary recirculation, such that occurring at the foot of a BFS. In this sense, the flow over a 25° BFR was observed to be analogous to that over the aforementioned two-dimensional hump [7,31], where no secondary recirculation was found. These observations on BFS and BFR flows were confirmed in preliminary experiments [56] and RANS simulations [57] conducted within the *ADaMant* project, in which a BFS and two BFR configurations were examined. In the presence of both the BFS and a 45° BFR, a TSB with main and secondary recirculation regions formed – although the size of the secondary recirculation region was markedly reduced for the 45° BFR, as compared to the BFS case. In contrast, no secondary recirculation was found in the presence of the 25° BFR.

Based on the available information on reference flow configurations, a 25° BFR was also considered for the present experimental work. This was motivated by the following aspects: the expected geometry-induced flow separation (directly at the top corner of ramp); the aforementioned analogy of the 25° BFR flow with the less understood hump flow; and the availability of results from the previous investigations introduced

above. The ramp was implemented on a flat-plate configuration designed to achieve a (globally) nearly-zero pressure gradient for most of the examined surface. The experiments were planned for a water tunnel with a relatively large test section, thus enabling the attainment of characteristic BFR Reynolds numbers relevant for practical aerodynamic applications ($Re_{xh} = U_\infty x_h/\nu > 10^6$, where x_h is the ramp location), while the freestream speed could be maintained low. The Large Water Tunnel of TU Braunschweig (GWB) [58] was selected for this scope; it allowed the conduction of experiments at a freestream speed reduced by a factor of about 8, as compared to matching Reynolds numbers in a wind tunnel with test section of similar size (the cross-section of the GWB test section is 1 m × 1 m). This provided suitable conditions for time- and space-resolved flowfield measurements via dense three-dimensional LPT by STB, aiming at the accurate determination of the distribution of mean flow velocity, acceleration, Reynolds stresses, and triple correlations. Especially the accurate information on the mean streamline curvature and on the full Reynolds stress sensor (including the Reynolds stress anisotropies) is essential for reliable turbulence model validation and modeling extensions, for example by improving a differential Reynolds stress transport model via a flow-feature adapted change of the Reynolds stress anisotropy [59]. Additionally, a three-dimensional flowfield characterization is crucial not only for the study of three-dimensional flow features characteristic of TSBs even in a statistically two-dimensional flow [7,8], but also for the improvement of turbulence models in numerical methods based on RANS equations and hybrid RANS/LES approaches, since such three-dimensional flow structures would challenge the RANS modeling assumption of a clear spectral separation in space (and time) of mean flow features and turbulence. Furthermore, an impact of three-dimensional flow structures on flow reattachment (which would otherwise be assumed to be essentially two-dimensional [38]) would raise the question in RANS modeling about the definition of a flow reattachment "location" in the presence of a reattachment line varying in the spanwise direction and – likely – also in time. To this aim, space- and time-resolved information on flow reattachment are necessary. STB can provide this information even close to the wall, but also a time- and space-resolved quantification of the flow impact directly on the surface (in terms of reattachment location, spanwise and temporal variation of the surface quantities, wall heat flux, and/or skin friction) is necessary for the advancement in physical understanding as well as for turbulence model validation and improvement. In air flows, infrared thermography [60] and OFI (see, e.g., [61]) can provide, in principle, surface information complementing the flowfield data from STB measurements, but these measurement techniques are not applicable in water flows. In contrast, TSP is well applicable in water [48–49,51–52,62–69], and its emerging capabilities for the study of flow separation and reattachment as well as for the estimation of the skin friction have motivated its combination with the STB technique in the present investigation. In line with its advantages for STB, the conduction of the experiments in the GWB water tunnel at low speed also allowed exploiting the capabilities of TSP to provide surface temperature fields with high spatial and temporal resolution. This enables the analysis of the spatial and temporal evolution of the surface temperature fluctuations, the evaluation of the celerity of propagation of temperature fluctuations (which is directly related to the skin friction), and the study of flow reattachment and of the wall thermal signature of the three-dimensional flow features.

In this work, the TSP measurements were performed upstream and downstream of the BFR, whereas Lagrangian particle tracks were obtained via STB in the regions upstream, over, and downstream of the BFR. These measurements were complemented by time-averaged surface pressure distributions obtained by means of pressure taps, which provided documentation of the streamwise pressure gradient changes over the flat plate (especially in the BFR region). In this manner, this new experiment complied with the superordinate goal of attainment of a high-quality experimental dataset for the validation and improvement of turbulence models used in numerical methods, while being at the same time adequate also for a comprehensive description of the examined BFR flow, thus supporting research for answering fundamental fluid dynamical questions.

Journal Pre-proofs

Specifically for this manuscript, a first main scope is the description of the experimental configuration implemented to study the considered BFR flow and of the application of the advanced optical measurement techniques to pursue the aforementioned superordinate goal. A second main scope of this work is the evaluation of the relevant, time-averaged flowfield and surface quantities with the high spatial resolution necessary for complying with the superordinate goal. The results comprise accurate distributions of the mean velocity and flow acceleration components, of the Reynolds stress sensor, and – for the first time for a reference TSB flow configuration – of the celerity of propagation of temperature fluctuations, which also enables the identification of the flow reattachment location and of its spanwise variation. As a further scope, the complementing STB and TSP data are compared to assess not only the mutual agreement of the reattachment locations identified from the fields of temperature fluctuation celerity and flow velocity, but also the spanwise distribution of near-wall, streamwise-oriented streaks of high/low streamwise velocity and of their thermal traces at the wall.

The article is structured as follows. The experimental setup, including the water tunnel, the examined flat-plate model and the applied measurement techniques, is described in Sec. 2. The experimental conditions are summarized in Sec. 3, whereas the acquisition and processing of the TSP and STB data are reported in Sec. 4. The obtained results are presented and discussed in Sec. 5. Finally, the conclusions of the current work are provided in Sec. 6. Further details on the experimental methodologies and on the data processing are given in Appendix A, whereas additional results are presented in Appendix B.

2 Experimental Setup

2.1 Large Water Tunnel of TU Braunschweig (GWB)

The measurements were carried out in the GWB water tunnel [58], a closed-circuit facility that can be pressurized up to 0.3 MPa to avoid cavitation effects. The test section has a square cross-section of 1 m sides (see Sec. 1) and a length of 6 m; it features exchangeable wall panels (12 for each side) and a slight divergence of the top and bottom wall (approx. 0.3°) to compensate for the growth of the wall boundary layer. The water flow is driven by a single-stage axial pump (1.5 m diameter) powered by a 160 kW electric motor, which enables the achievement of freestream velocities up to $U_\infty = 6$ m/s in the test section. Additionally, the water temperature can be increased up to 40 °C to further increase the Reynolds number.

2.2 Flat-Plate Model Configuration and Model Installation

The measurements were conducted on a two-dimensional (i.e., spanwise-invariant) flat-plate model with symmetric cross-section, as sketched in Figure 1. The plate leading edge was shaped as a super-ellipse [70] with an aspect ratio of 6:1, in order to reduce the magnitude of the pressure minimum in the leading-edge region and thus reduce the risk of premature flow separation. The trailing-edge region was designed with a sharp edge and an angle of approx. ±8.2° with respect to the freestream, aiming at the avoidance of unsteady effects due to vortical structures that would otherwise originate from a large separation region at a trailing edge with blunter geometry. The remaining model surfaces were flat, except for the aforementioned 25° BFR. This was installed at the streamwise location $x_h = 1.134$ m and had a height $h = 8$ mm. In this work, x is the streamwise coordinate (positive in the downstream direction starting from the model leading edge), y the wall-normal coordinate (positive upward starting from the surface downstream of the BFR),

and z the spanwise coordinate (positive starting from the centerline to the model port side). The corresponding streamwise coordinate in the BFR reference system is $X = x - x_h$, while Y and Z are equivalent to y and z, respectively.

In analogy with the preceding wind-tunnel experiment [56,57], the model design aimed to achieve a ratio $h/\delta_{99} \sim 0.4$ at x_h for the examined Reynolds number, where δ_{99} is the boundary-layer thickness at the ramp location, but in the absence of the BFR. The relative step height was smaller than that examined, e.g., in [23,29], where $h/\delta_{99} > 2$, but it was designed to be in line with that studied in the BFS flow of [14]. A BFR with this non-dimensional step height was expected to induce a relatively thin TSB, which would be representative for TSBs occurring in practical aerodynamic applications, such as in the presence of shock-induced separation or in the trailing-edge region of transonic aircraft wings.

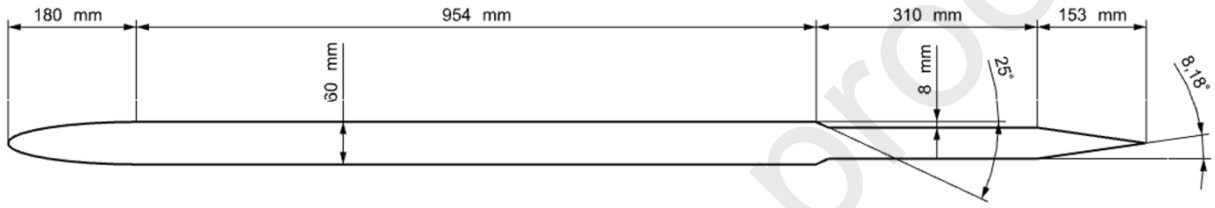

Figure 1: sketch of the flat-plate model with 25° backward-facing ramp (side view).

The experimental configuration was designed with a main body and exchangeable modules for the installation of the different measurement techniques. The model surface with exchangeable modules was the main surface of interest and is named *measurement surface* in this work. The opposite surface is named *rear surface*. The main body of the model was equipped with a main row of pressure taps for the measurement of the surface pressure distribution, as will be described in Sec. 2.3.1. The three exchangeable modules were:

- a *pressure module* for the additional measurement of the pressure distribution upstream and downstream of the BFR via supplementary pressure taps;
- a *TSP module* for surface temperature measurements upstream and downstream of the BFR;
- and an *STB module* for LPT upstream, over, and downstream of the BFR.

The measurement systems based on these three modules are discussed below in Secs. 2.3.1–2.3.3.

The flat plate was mounted vertically in the test section and spanned the whole test-section height, as shown in Figure 2. (In this photograph, the TSP module was installed in the model.) The BFR was positioned at a streamwise location of approximately $x_{WT} = 3.25$ m from the beginning of the test section. A panel specifically designed for optical access of the STB and TSP measurement techniques was installed at the GWB side wall, in front of the modules region – see Figure 2. Further details on the flat-plate model and on the optical access panel are provided in Appendix A.1 and A.2, respectively.

Journal Pre-proofs

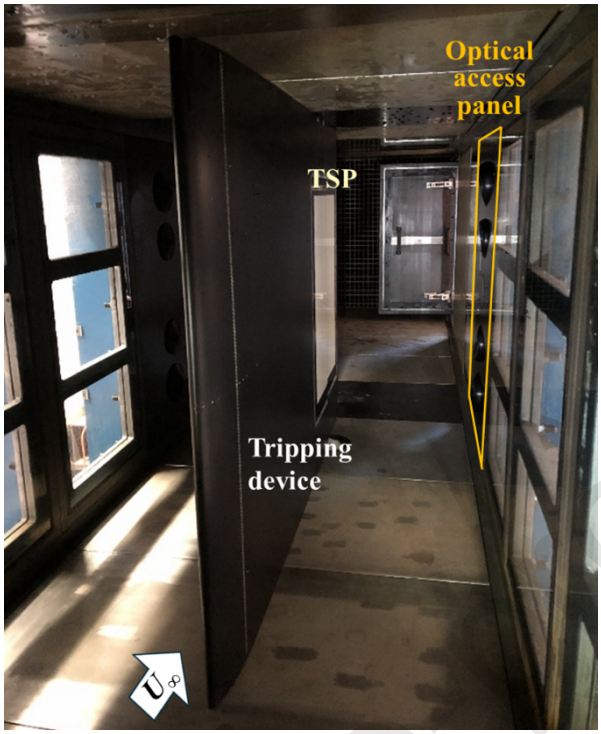

Figure 2: photograph of the flat-plate model with TSP module installed in the GWB test section. View in flow direction on the measurement surface. Information on the indicated tripping device, applied at $x_k = 0.13$ m for transition forcing, is provided in Sec. 3.

2.3 Experimental Techniques

This section describes the implementation of the measurement techniques for the measurement of the pressure distribution on the model surface (pressure taps, Sec. 2.3.1) and for the investigation of the boundary-layer evolution in the presence of the BFR (TSP and STB in Secs. 2.3.2 and 2.3.3, respectively). In the case of TSP and STB techniques, their optical setups are also presented in the corresponding sections, while the acquisition and processing of the TSP and STB data are described in Sec. 4.

2.3.1 Pressure taps

As introduced in Sec. 2.2, the main body of the model and the pressure module were equipped with pressure taps; the total number of pressure taps with mounted pressure module was 62. Most of the pressure taps (48) were installed on the measurement surface, with the remaining 14 taps installed in the rear model surface. On both model surfaces, the majority of the pressure taps was arranged along the centerline; nevertheless, 4 pressure taps (2 for each model surface) were installed at $x = 0.14$ m and at a spanwise location $z = \pm 0.35$ m, in order to obtain an indication on spanwise variations of the pressure distribution on the leading-edge area.

All pressure taps had a diameter of 0.8 mm. They were connected through tubings with a diameter of 2 mm to the GWB pressure measurement system [58], which sensors have an accuracy of ±50 Pa. The pressure

data were acquired at 10 Hz for each sensor over a time window of 10 s, and eventually time-averaged to obtain the surface pressure distribution.

2.3.2 Temperature-Sensitive Paint (TSP)

When TSP is applied in low-speed flows such as that examined in this work, the temperature variations induced by the flow on the investigated surface are typically too small to be detected [47,71]. Nevertheless, several methods have been successfully implemented in previous work to enhance these flow-induced temperature differences [40,47–52,62–69,71–80], thus accomplishing in the measurement of the surface temperature distribution with high spatial resolution. Among these methods, a current-carrying carbon fiber layer (Carbon-Fiber-Reinforced Plastic, CFRP) was chosen as electrical heating system to be integrated beneath the TSP coating, in a manner analogous to that described in [50,65–66].

For the integration of the TSP coating [81] and of the CFRP layer, the TSP module was designed with two laminates embedded into an aluminum frame, which comprised also the BFR. This latter was installed as metallic component in order to guarantee the achievement of the required geometry, and in particular the sharpness of the BFR corners. A sketch and a photograph the TSP module are shown in Figure 3 – left and right, respectively. Each laminate supported one TSP measurement field: one TSP field (*TSP 1*) was placed upstream of the BFR, whereas the other one (*TSP 2*) was downstream of the BFR. The dimensions of the TSP fields are reported in Figure 3 (left), whereas details on the two laminates are provided in Appendix A.1.

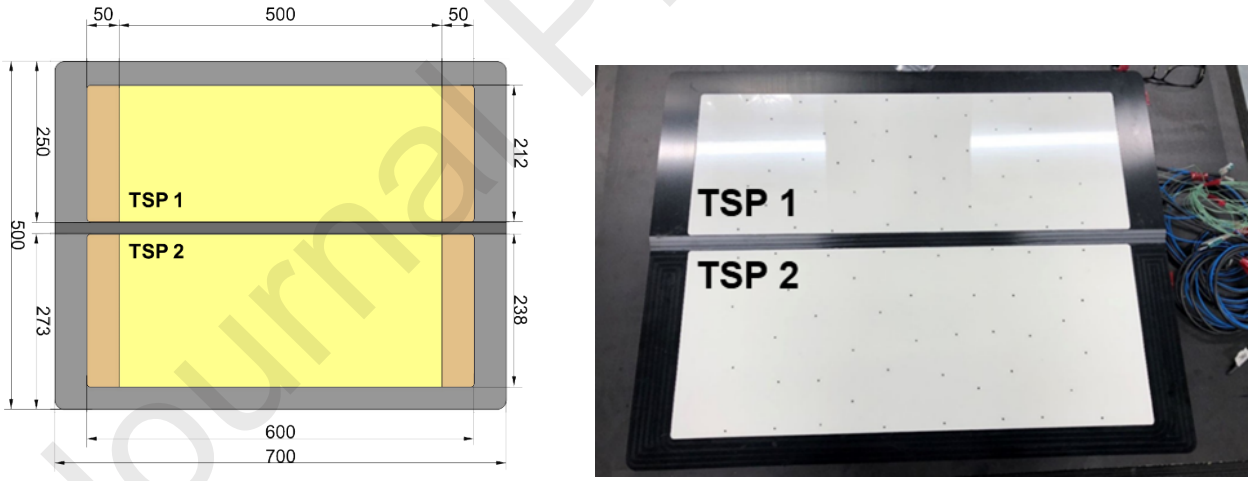

Figure 3: top views of the TSP module. The top and bottom TSP fields are upstream and downstream of the BFR, respectively. Left: sketch with distances in mm. The copper-based contacting strips for the CFRP heating layer are shown in brown, while the effective TSP areas are shown in yellow. Right: photograph of the TSP module, with the TSP areas appearing as pale-yellow coatings. The black circular markers for TSP image processing (see Appendix A.4) are also visible.

Journal Pre-proofs

The experimental setup for the TSP measurements is sketched in Figure 4. The TSP hardware consisted of one high-speed camera and three in-house systems of Light-Emitting Diodes (LEDs). The camera was a Complementary Metal-Oxide-Semiconductor (CMOS) Phantom v2640 camera, which has a 12-bit dynamic range and was operated at full resolution, i.e., with a 2048 × 1952 pixels^2 image sensor. The camera was equipped with a Nikkor lens of 35 mm focal length, and with an optical band-pass filter for the wavelength range of 590–670 nm, which was installed in front of the lens. This latter allowed the light emitted by the TSP to be captured (see Appendix A.1), while at the same time blocking light at lower and higher wavelengths. The TSP data were acquired over a mid-span region (streamwise × spanwise) of approximately 300 × 285 mm^2, covering portions of both TSP fields.

The used LEDs had a central emission wavelength of λ_{peak} = 395 nm. Optical band-pass filters, blocking light at λ < 350 nm and λ > 420 nm, were placed in front of the LEDs in order to avoid an influence on the acquired luminescent images. The LED systems were cooled using vortex tubes.

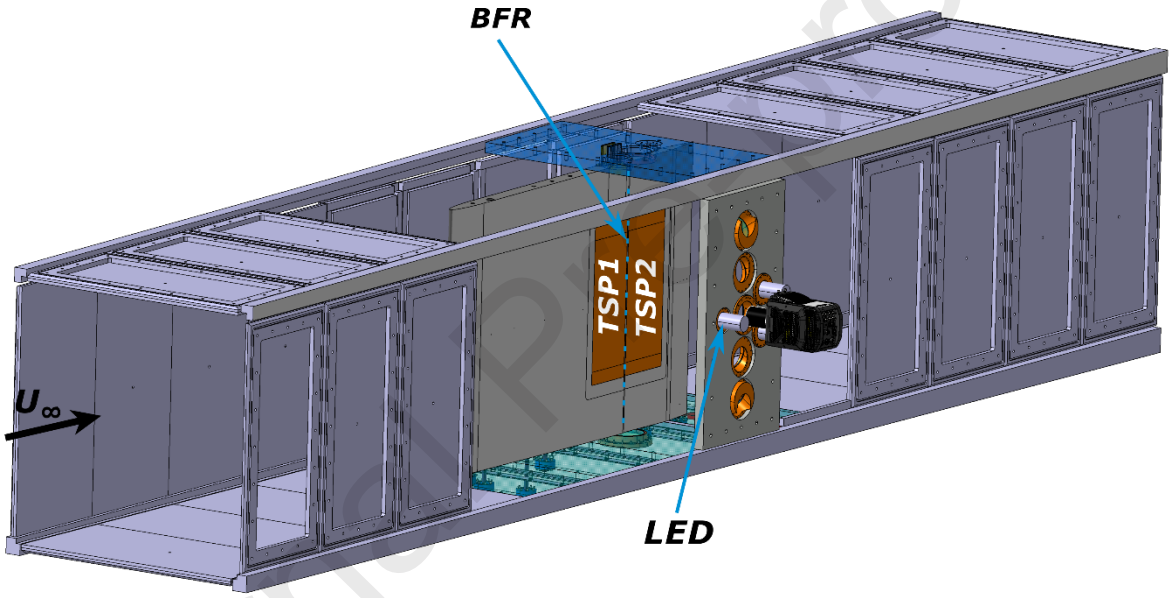

Figure 4: sketch of the experimental setup for the TSP measurements.

2.3.3 Lagrangian Particle Tracking (LPT) via Shake-The-Box (STB)

The STB module was composed of a glass insert embedded into an aluminum frame, as shown in Figure 5. The glass insert was designed to avoid wall reflection of the illumination light for the STB measurements. Its dimensions are reported in Figure 5 (left). It should be emphasized here that the BFR was directly manufactured into the glass by using a triangle prism and refractive-index matching glue. The glass insert was fixed into the aluminum frame via black silicone.

Submitted to the Special Issue of *Experimental Thermal and Fluid Science* (*ETFS*) dedicated to the 6th International Conference on Experimental Fluid Mechanics (ICEFM). Revision R1

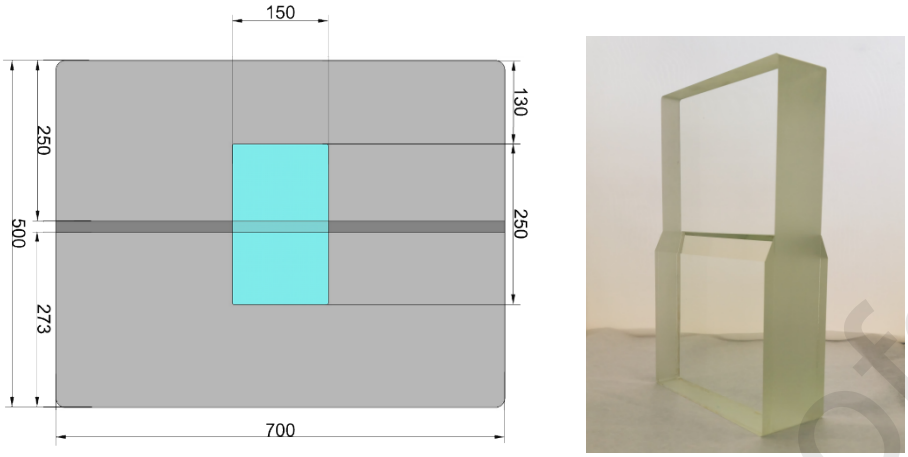

Figure 5: top views of the STB module. The top and bottom areas are upstream and downstream of the BFR, respectively. Left: sketch with distances in mm, where the glass insert is shown in cyan. Right: photograph of the glass insert for the STB module.

An STB system for three-dimensional flow characterization needs at least 3 cameras for triangulation; as shown in Figure 6, five CMOS cameras were employed in this experiment to enhance measurement accuracy: one Phantom T4040 and four Phantom v2640 cameras (the latter were of the same type as that used for the TSP measurements, see Sec. 2.3.2). The cameras were arranged vertically in an in-line configuration behind the optical access panel (see Figure 6). All cameras pointed at the same measurement volume and enabled the acquisition of STB data in a volume of approximately $85 \times 90 \times 15$ mm^3 (streamwise × spanwise × wall-normal) around and downstream of the BFR. This was accomplished by mounting Zeiss Macro Planar lenses with 100 mm focal length in front of the cameras; additionally, 2× teleconverters were used for the two outer cameras with longest viewing distances. Scheimpflug adapters were used to keep all particles in focus in the wall parallel volume(s) . In fact, the STB measurement volume was spatially and temporally subdivided into two subvolumes, in order to increase the particle concentration within each subvolume (*particles per volume*) while limiting the imaged particle density (*particles per pixel*), following the approach proposed in [46]. Each subvolume covered a wall-normal distance of approximately 8 mm, with an overlap of about 1 mm between the two. The two-stage scanning process implemented in this work (see Sec. 4.2 and Appendix A.3) was enabled by alternate illumination of the particles in the two subvolumes using a dual-head Nd:YAG (532 nm wavelength) nanosecond-pulsed high-speed laser (Photonics Industries DM200 series). As sketched in Figure 6, the two laser beams were spatially separated and guided through suitable lenses and mirrors to enter the GWB test section from the bottom-wall window (see Appendix A.2) and thus generate the two collimated subvolumes.

Spherical polyamide particles [82] with a density of 1,020 kg/m^3 and an average diameter of 20 µm were used in this work as almost-neutrally buoyant seeding for the STB measurements.

Further details on the STB measurement system are provided in Appendix A.3.

Submitted to the Special Issue of *Experimental Thermal and Fluid Science* (*ETFS*) dedicated to the 6th International Conference on Experimental Fluid Mechanics (ICEFM). Revision R1

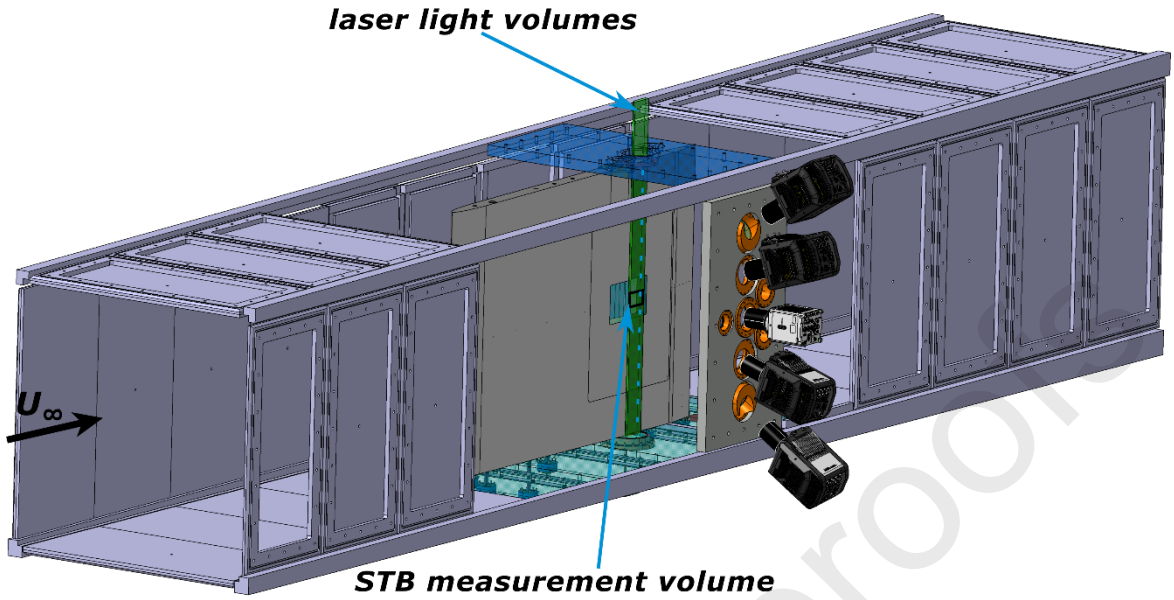

Figure 6: sketch of the experimental setup for the STB measurements.

3 Experimental Conditions

This work focuses on a Reynolds number based on the streamwise BFR location from the model leading edge of $Re_{xh} = 1.2 \cdot 10^6$. The corresponding Reynolds number based on the BFR height was $Re_h = U_\infty h/\nu = 8{,}800$, as summarized in Table 1. The examined flow condition matched one of those studied in the preceding wind-tunnel experiment [56,57] both in terms of Re_{xh} and Re_h. Note that these BFR Reynolds numbers were the same for all three test campaigns conducted with the pressure, TSP, and STB modules, while the freestream speed U_∞ had to be adjusted depending on the fluid temperature for the respective water-tunnel entry. Furthermore, the GWB water tunnel was pressurized to 0.16 MPa for the TSP measurements, while the STB measurements were conducted at atmospheric conditions. The pressurization enabled a reduction of the amount of air bubbles advected by the water flow, which would have otherwise affected the light path between the optical setup and the TSP surfaces. An example of such an impact on the TSP data is shown later in Sec. 5.1 (Figure 10, top-right). In contrast, the impact of the air bubbles on the STB measurements was negligible because of the focused light illumination close to the model surface. The evolution of the turbulent boundary layer was not affected by the pressurization, as demonstrated by the reproducibility of the surface pressure distributions in the test campaign using the pressure taps module, where measurements were conducted at both pressure levels.

Table 1: experimental conditions for the three different water-tunnel entries.

Used module	**Freestream speed [m/s]**	**Re_{xh}**	**Re_h**	**Tunnel pressure [MPa]**
Pressure	1.3	$1.2 \cdot 10^6$	8,800	0.10; 0.16

TSP	1.1	$1.2 \cdot 10^6$	8,800	0.16
STB	1.0	$1.2 \cdot 10^6$	8,800	0.10

A tripping device was applied at a streamwise distance x_k = 0.13 m on both model surfaces in order to force transition, thus enabling investigations of a fully developed TBL and enhancing flow symmetry over the flat plate. The tripping device was a zigzag strip (3D turbulator tape) with a tooth angle of 60° and a distance between teeth of 6 mm [83]. The thickness of the strip was 0.205 mm. As shown in Figure 2 for the measurement surface, the tripping strip was applied in the spanwise direction, i.e., with its main axis perpendicular to the freestream. The strip was applied using an epoxy-based glue, leading to a final thickness of the tripping device of approx. k = 0.3 mm.

4 Optical Data Acquisition and Processing

This section presents the procedures for the acquisition of the time-resolved TSP and STB images (Secs. 4.1 and 4.2, respectively) and the corresponding image processing steps to obtain the fields of the relevant quantities.

4.1 TSP Data

The TSP images were acquired at a frequency of 1 kHz (with an exposure time of 0.99 ms). The TSP image acquisition procedure followed a standard approach for intensity-based TSP measurements (see, e.g., [47–48,50,71], among others); it comprised TSP image sets with inactive (*Ref* images) and activated heating (*Run* images), thus enabling an enhancement of the flow-induced temperature differences (see Sec. 2.3.2). The electrical power density applied to the CFRP layers was 3 kW/m^2 for both TSP fields, in order to ensure consistency in the thermal conditioning of the TBL undergoing separation. Details on the TSP data acquisition procedure and on the initial processing to attain time-resolved surface temperature maps are provided in Appendix A.4. These surface temperature maps were still affected by noise generated during the excitation/emission process, as expected in luminescence-based measurements. The nature of this Additive, White, Gaussian Noise (AWGN) enables effective denoising via filtering techniques such as those presented in [48,51–52].

The present measurements were however affected by additional, non-AWGN disturbances, which required ad-hoc treatment. The origins of these non-AWGN disturbances were retraced in the used high-power LED systems. As discussed in [84], high-power LEDs are affected by a loss of efficiency due to warming up, which leads to a reduction in illumination intensity over time. This is particularly pronounced after activating the LEDs; for this reason, the acquisitions of both *Ref* and *Run* sets of TSP images were started 5 s after LED activation, such that the temporal gradient of the LED illumination intensity was reduced. This remaining temporal change in LED illumination intensity resulted in an apparent temperature drift in the time series of the TSP data, as shown in Figure 7 (left); here, the blue line corresponds to the temporal evolution of the streamwise- and spanwise-averaged surface temperature on the TSP field downstream of the BFR, obtained after an initial spatial filtering step (described further below). As can be seen in this figure, the apparent increase in temperature after a measurement time of 12.5 s was about 0.1 K. Furthermore, a number of spikes was observed in the temporal evolution of the TSP signal; because of their

impulsive nature (apparently disconnected from spatial temperature changes), their origin may be attributed to instantaneous instabilities of the LED emission (possibly induced by electrical interference within the facility). Based on this conjecture, a further step for spikes removal was introduced into the data filtering chain: the drift profile (blue curve) was approximated by a 2nd order polynomial function (black dashed line in Figure 7, left), and the spikes were removed using a compensation temperature map, which was added to the original temperature map. The compensation map was obtained as mirror of the original temperature map about the approximation function for each time instant affected by the spikes.

In summary, the data filtering chain comprised the following steps, which intermediate (final) results in terms of streamwise- and spanwise-averaged surface temperature are presented as lines of different colors in Figure 7 (left):

- Spatial filtering using a deformed, edge-preserving Gaussian filter [48] (blue profile);
- Butterworth low-pass temporal filtering with cut-off frequency of 300 Hz and spikes removal step, as described above (red profile);
- Correction for the apparent temporal drift by subtraction of the aforementioned approximation function (black solid profile).

Details of this final temperature profile obtained at the end of this process are shown in Figure 7 (right) for two different time windows of 2 s (bottom) and 50 ms (top). In particular, it should be noted in the top-right figure that the captured temperature fluctuations were well within 0.01 K. The effectiveness of the data filtering chain in improving the signal-to-noise ratio of the instantaneous temperature maps is illustrated in Figure 8 for the TSP field downstream of the BFR, where the left and right figures correspond to the unfiltered and final surface temperature distributions, respectively. After application of the filtering chain, flow-induced thermal footprints were revealed even in such instantaneous temperature maps: a colder region close to end of the ramp (blue region up to $X = x - x_h \sim 55$ mm), and streamwise-oriented streaks further downstream. These footprints will be discussed in Sec. 5.

The resulting temperature resolution of the surface temperature maps was below 0.001 K, with a spatial resolution of 0.145 mm in both streamwise and spanwise direction.

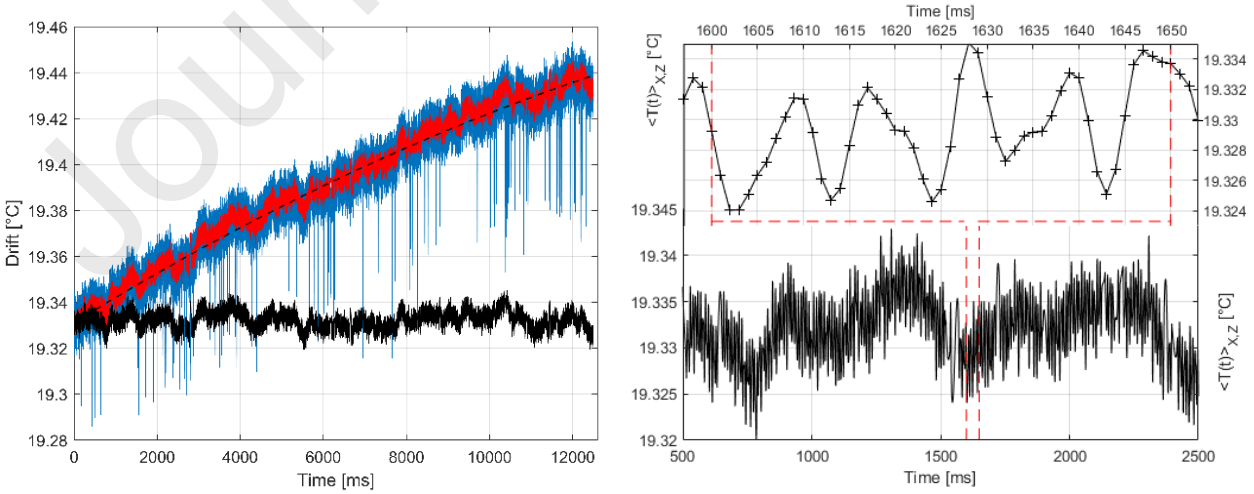

Figure 7: left: temperature drift over the *Run* data series for the TSP field downstream of the BFR, obtained as average along the streamwise and spanwise directions $<T>_{XZ}$. Blue line: original data, after spatial filtering; red line: after temporal filtering and spike removal; black solid line: after removal of the apparent temperature drift, indicated as a black dashed line approximating the drift profile. Right. details of the resulting profile (black solid line in the left figure) for time windows of 2 s (bottom) and 50 ms (top), showing characteristic temporal scales of about 0.5 s and 10 ms, respectively.

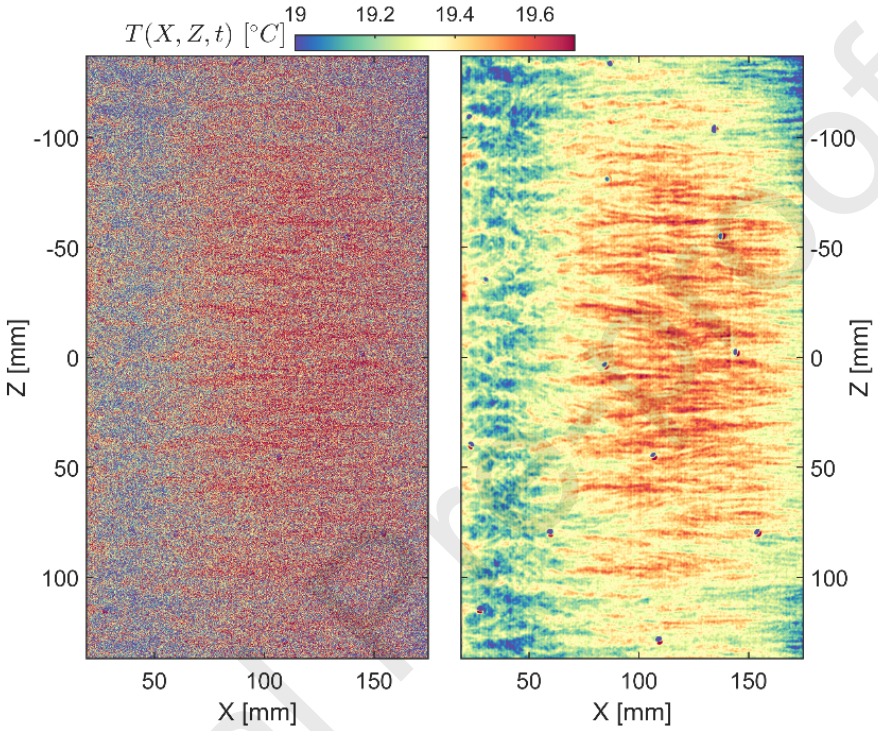

Figure 8: instantaneous surface temperature maps for the TSP field downstream of the BFR. Left: unfiltered; right: after application of the filtering chain.

For the study of flow separation induced by the BFR, two different approaches were applied for the determination of the time-averaged reattachment location X_R from surface temperature data. The first, more straightforward approach is based on the identification of the minimum of the time-averaged surface temperature profile in the streamwise direction ($X_{R,T}$) [40]; the other approach is based on the observations of the near-wall behavior of the perturbations of flow quantities, and in particular of the temperature, which is assumed to behave as a passive scalar. In the vicinity of a rigid surface, the flow mean velocity approaches zero, while perturbations of the flow quantities propagate at a velocity that is in relationship with the friction velocity. Since this behavior is similar to that of a wave, the term *celerity* is used in this work to define this propagation velocity of the perturbations of flow quantities. For canonical flows, direct relationships were reported in the literature between the friction velocity and the propagation celerity of velocity perturbations $\vec{U}_{u_i}$ (where u_i are the velocity components) [85,86], as well as between the propagation celerities of velocity and temperature perturbations [87]. If these relationships are known, such as in the case of the turbulent flume in that latter study, the friction velocity can be evaluated when the propagation celerity of temperature

perturbations $\vec{U}_T$ is known. As discussed in [48–52,67], the traces of the temperature fluctuations at the wall T' can be measured via TSP when enhanced by an imposed heat flux, e.g., via the current-carrying carbon fiber layer described in Sec. 2.3.2. The analysis of the time-resolved T'-maps obtained from the TSP data can provide maps of $\vec{U}_T$ (with streamwise and spanwise components U_T and V_T, respectively), thus enabling the determination of skin-friction fields through the relationship between $\vec{U}_T$ and friction velocity, if this latter is known. Following the approach proposed in [48–52,67,88], which is adapted from the approach to obtain $\vec{U}_{u_i}$ from [89,90], the time-averaged $\vec{U}_T$ was determined in this work by minimizing the difference between the experimentally observed behavior of the temperature fluctuations and that predicted by the Taylor Hypothesis of "frozen turbulence" [91] (*TH approach*). Although a relationship between $\vec{U}_T$ and friction velocity is not available yet for the examined non-canonical flow, the streamwise distribution of U_T can be used for the determination of the reattachment location downstream of the BFR, which is identified at the location corresponding to the zero-crossing of U_T ($X_{R,UT}$, see Sec. 5.1).

4.2 STB Data

As introduced in Sec. 2.3.3, a two-stage scanning process [46,92] was employed in the STB data acquisition. The laser was operated in double-pulse mode at a frequency of 3 kHz, while the cameras were operated at double the laser frequency, i.e., at f_{acq} = 6 kHz. In this manner, the cameras captured the lower measurement subvolume in every even frame and the upper volume in every odd frame, while each camera recorded the entire volume. The two laser beams were temporally separated by a time delay corresponding to the inverse of the camera acquisition frequency. Due to the huge difference in temporal scales characteristic of the examined separated TBL, the images were acquired in small temporal *chunks*, rather than in a long time series. In this manner, a large number of statistically independent boundary-layer samples were recorded. Each chunk comprised 30 images of consecutive time-steps, and 100 chunks were acquired for each acquisition series. In total, 28 series were acquired, corresponding to 2,800 chunks. The data acquisition parameters of the STB measurements are summarized in Table 2.

Table 2: STB data acquisition parameters.

Number of series	**f_{acq} [kHz]**	**Number of images per series**	**f_{chunk} [Hz]**	**Δt [µs]**	**Camera resolution [pixels^2]**
28	3 (× 2)	30 × 100 × 2	2	167	2048 × 1952

The STB data processing for the lower and upper subvolumes was carried out via Variable Time-step STB (VT-STB) [45] and standard STB processing, respectively. Details on the STB data processing are provided in Appendix A.3. The obtained tracks were temporally fitted via *TrackFit* filtering using 3rd order B-splines for each dimension in space; this was accomplished with filter strength optimized for each component, as determined via the position spectrum of the raw tracks [93]. The particle velocities and accelerations were then estimated by first and second temporal derivatives along the 3rd order B-splines. In total, about 90,000

instantaneous 3D velocity and acceleration vector fields along approx. 250,000 particle tracks per time-step were obtained.

Assuming statistically steady and two-dimensional flow conditions, time- and spanwise-averaged statistics of all three-components of velocity and acceleration, as well as the corresponding Reynolds stresses and triple correlations were obtained from the reconstructed, three-dimensional particle trajectories via a bin-averaging approach [92,94]. This approach was applied here within bins of $\Delta x \times \Delta y = 125 \times 125$ µm^2 size, which covered the whole examined spanwise extent. A convergence study for the statistics showed a mean deviation of the different velocity components well below 0.1 % of the freestream velocity. Time-averaged flow reattachment was identified from the mean velocity fields by determining the streamwise location downstream of the BFR with zero streamwise velocity component close to the wall ($X_{R,u}$).

Furthermore, the instantaneous flowfield snapshots were also evaluated to identify three-dimensional turbulent flow structures. This was enabled by Navier-Stokes regularized interpolation and data assimilation conducted via the DLR code *FlowFit3* [93,95]. The inputs for *FlowFit3* were the particles velocities and accelerations. This provided a continuous flowfield representation within a grid of three-dimensional cells (spaced by 0.5 mm) using mixed 3rd- and 4th-order B-splines. Examples of the quality of the attained results for the whole STB measurement volume are provided in Appendix A.3 and in the Supplementary Material, whereas the next section will focus on wall-parallel slices.

5 Results and Discussion

An overview of the boundary-layer development on the examined model is provided by the measured surface pressure distribution, which is shown in Figure 9 as pressure coefficient $c_p = 2(p - p_\infty)/(\rho U_\infty^2)$ vs. streamwise coordinate x. Here, p and p_∞ are the local and freestream static pressure, respectively, and ρ the water density. The orange and gray vertical lines indicate the locations of the tripping device (x_k) and of the BFR (x_h), respectively. As can be seen in the figure, the boundary layer accelerated over the super-elliptic leading edge, and encountered an adverse pressure gradient just downstream of x_k; by placing the tripping device at this location it was avoided that the possibly still laminar boundary layer underwent separation. Further downstream, in the main plate region at approx. 0.3 m < x < 1.1 m, the streamwise pressure gradient was nearly zero. In the region around x_h, the local changes in pressure distribution were induced by the influence of the BFR on the TBL development, leading to a favorable pressure gradient immediately upstream of the BFR, an adverse pressure gradient just downstream of the BFR, and again a favorable pressure gradient. Finally, a recovery of the nearly-zero pressure gradient was approached at $x \sim 1.3$ m, but not fully achieved because of the impact of the trailing-edge region (see Figure 1), which induced further variations in the pressure distribution. Reasonable agreement was found for the pressure distributions measured on the two model surfaces, even for the regions with more pronounced pressure gradients. This result indicates an essential symmetry of the flow development over the flat plate. The measurements of the additional pressure taps at $z = \pm 0.35$ m (green triangles) support the assumption of quasi-two-dimensional flow at least for the central spanwise area, since their data are in line with those measured along the model centerline. Because of the very limited number of pressure taps available far from the centerline, however, the evaluation of the flow two-dimensionality over the front model areas is not conclusive; nevertheless, clearer information on the two-dimensionality of the TBL upstream and downstream of the BFR will be provided by the TSP results in Sec. 5.1. In that section, also the results of the TH approach (see Sec. 4.1) applied to the time-resolved TSP data will be presented. The flowfield statistics obtained from the STB data analysis are provided in Sec. 5.2. The TSB induced by the BFR is discussed in Sec. 5.3 based on the TSP

and STB results and their comparison with literature data. Three-dimensional flow structures and wall thermal traces, revealed by the time-resolved STB and TSP data, will be analyzed and discussed in Sec. 5.4.

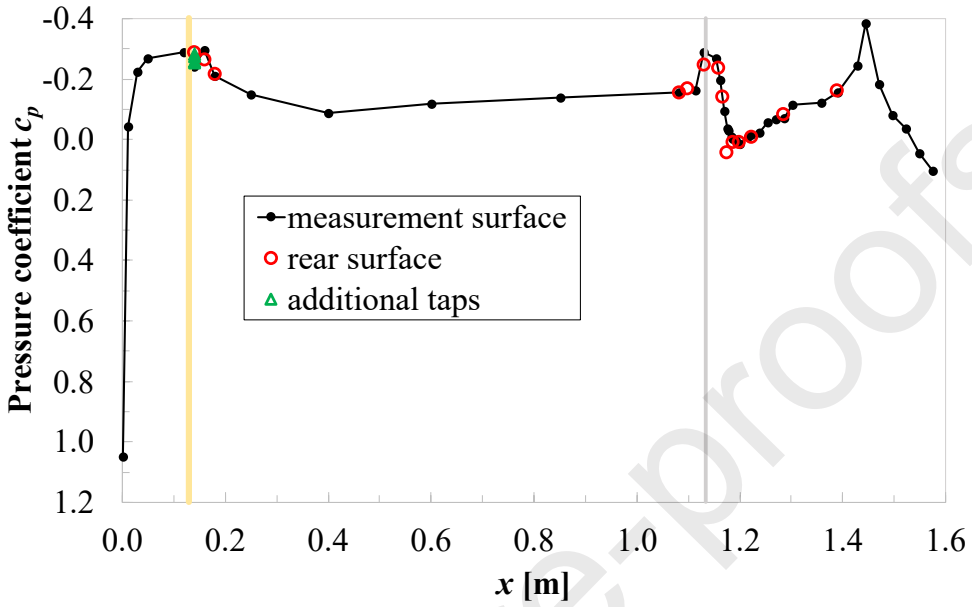

Figure 9: (time-averaged) surface pressure distribution measured using pressure taps. The orange and gray vertical lines indicate the locations of the tripping device and of the BFR, respectively.

5.1 Surface Temperature and Temperature Fluctuation Celerity Fields

The first level of results obtained from the analysis of the TSP images is the time-averaged temperature distribution $\overline{T}$, which is shown in Figure 10 (top-left), with the flow from the left. As can be seen in this figure, the $\overline{T}$-distribution in the central spanwise region (at approx. -75 mm < z < 75 mm, comprising also the measurement region in the STB experiment) were found to be essentially two-dimensional both upstream (X < 0) and downstream of the BFR (X > 20 mm). Towards the corners of the imaged area, an apparent temperature reduction, likely due to vignetting effects, was observed. Note that this was not due to spatial changes in the imposed heat flux, as proven in preliminary TSP image acquisitions with a lens of 28 mm focal length. Additionally, a flow-independent, fabric-like pattern (characterized by vertical and horizontal lines) can be seen superimposed on the flow-induced temperature distribution. This pattern probably originated from the CFRP layer when the heating system was activated, and was not sufficiently mitigated by the screen layer and top GFRP layer comprised in the laminates (see Appendix A.1). In spite of this, the evaluation of the $\overline{T}$-distribution in the streamwise direction showed a broad temperature minimum at $X \sim$ 32–42 mm, as will be seen even more clearly in the time- and spanwise-averaged temperature profile presented further below in Figure 11 (center and bottom-right). As introduced in Sec. 4.1, the minimum of the time-averaged surface temperature profile in the streamwise direction was reported to correspond to the reattachment location in earlier work on a BFS flow [40]. The transferability of this observation to the present results will be discussed later in this section.

The processing of the time-resolved TSP data provided the maps of temporal standard deviation σ_T (shown in Figure 10, top-right) and of the traces of the temperature fluctuations at the wall T', an example of which is presented in Figure 10 (bottom). This latter result reports an instantaneous map (snapshot) of surface temperature fluctuations, defined as the difference between instantaneous temperature maps and the time-averaged temperature map of the data series ($T' = T - \overline{T}$). A video showing a temporal series of temperature maps (6,000 snapshots) is available as Supplementary Material (Video-1: Tfluctuations.mp4). Note that the σ_T map is only marginally affected by the flow-independent disturbances described above with regard of the time-averaged temperature distribution (Figure 10, top-left), while their impact essentially disappears in the T' maps. As an example of a remaining disturbance with more significant impact on the standard deviation map, the influence of an air bubble is visible in Figure 10 (top-right) as an apparent high-σ_T streak close to the centerline (relatively straight upstream of the BFR and meandering further downstream). This influence was then removed in the further analysis of the TSP data.

The streamwise extent of the spanwise-oriented region of large temperature standard deviation (between the foot of the BFR and $X \sim 50$ mm) is also in line with the distribution of the root mean square of the surface temperature in the BFS flow experiment of [40], which was found to have a maximum upstream of the flow reattachment location and to maintain significantly higher values also slightly downstream of it.

The instantaneous temperature maps enable the analysis of the flow-induced thermal signatures on the examined surfaces. The inspection of the TSP results in Figure 10 (bottom) and in Video-1 shows three different patterns of traces of temperature fluctuations at the wall: one in the region upstream of the BFR, a second one downstream of the BFR up to approx. $X = 40$ mm, and a third one further downstream. Nevertheless, the instantaneous temperature maps do not show appreciable spanwise modulation in any of the three regions, thus confirming the quasi-two-dimensionality of the global TBL thermal signature at the wall. In the regions at $X < 0$ and at approx. $X > 40$ mm, the wall thermal traces appear to propagate downstream in a streaky arrangement, which will be discussed in Sec. 5.4. A substantially different pattern is visible in the region at approx. 20 mm $< X <$ 40 mm, where the wall thermal traces appear to displace upstream, i.e., towards the BFR. This difference in the propagation direction of the wall thermal traces provides an indication of the occurrence of a ramp-induced TSB extending up to $X \sim 40$ mm.

Journal Pre-proofs

Submitted to the Special Issue of *Experimental Thermal and Fluid Science* (*ETFS*) dedicated to the 6th International Conference on Experimental Fluid Mechanics (ICEFM). Revision R1

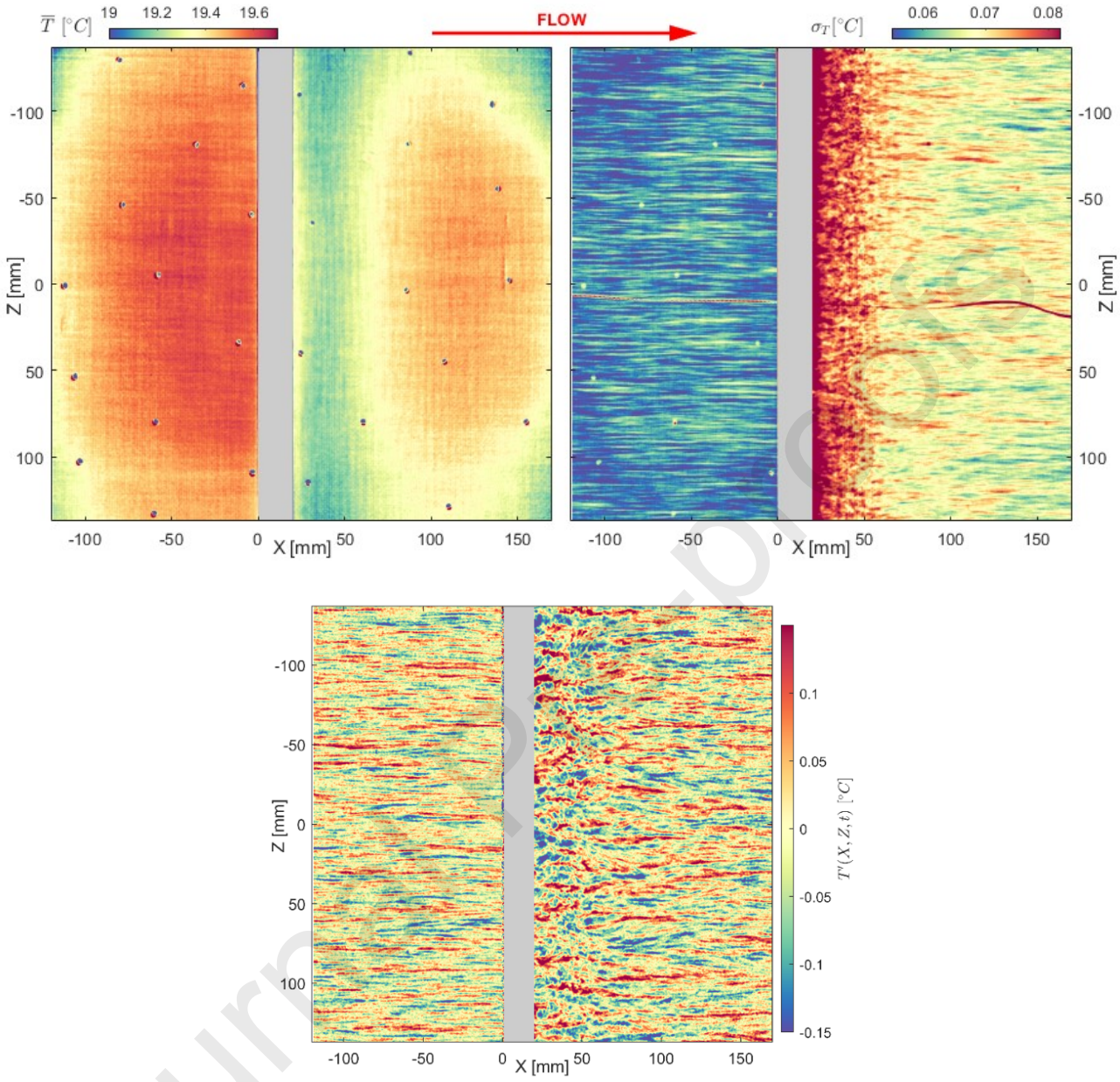

Figure 10: time average (top, left) and temporal standard deviation (top, right) of the surface temperature distribution. Bottom: instantaneous temperature distribution. All three figures refer to the surface temperature data on the TSP fields upstream and downstream of the BFR, with the (main) flow from the left. The map of temperature fluctuations (T') was obtained as the difference between instantaneous temperature maps and the time-averaged temperature map ($\overline{T}$) of the data series (i.e., the top-left figure).

A quantitative study of the flow evolution downstream of the BFR is enabled by the celerity of propagation of temperature fluctuations ($\vec{U}_T$), as introduced in Sec. 4.1. The TH approach was applied to the time-resolved temperature maps to obtain the time-averaged map of $\vec{U}_T$. Results are provided in Figure 11: the left figure reports the field of wall streamlines of $\vec{U}_T$ (i.e., obtained by combining its streamwise and spanwise components, U_T and V_T), whereas the spanwise-averaged profile of U_T downstream of the BFR is

shown in the center figure, where also the spanwise-averaged distribution of the time-averaged wall temperature (from Figure **10**, top-left) is presented as a red line. The wall streamlines of $\vec{U}_T$ are analogous to the skin-friction lines (i.e., the limit streamlines when the wall-normal distance tends to zero [96]), and therefore provide a topological description of the flow at the surface. The topology reported in Figure 11 (left) clearly shows an inversion of the $\vec{U}_T$ wall streamlines at $X \sim 40$ mm, thus confirming a change in the direction of the transport of wall temperature fluctuations; furthermore, it confirms the quasi-two-dimensionality of the (time-averaged) TBL wall signature for all three examined regions. The spanwise-averaged profile of U_T (Figure 11, center) shows negative U_T-values at approx. 20 mm < X < 40 mm and positive values further downstream. Although the relationship between $\vec{U}_T$ and friction velocity is not known in quantitative terms for the examined non-canonical flow, such relationship enables a physics-based identification of separated and attached flow areas, as discussed in [48–52], among others. The critical line of divergence of the $\vec{U}_T$ wall streamlines, observed in Figure 11 (left), corresponds to the time-averaged line of flow reattachment downstream of the BFR. Moreover, no secondary recirculation was found: it would have led to the appearance of an additional critical line of converging $\vec{U}_T$ wall streamlines, which is not observed in the present result.

The time- and spanwise-averaged location of flow reattachment X_R can be further quantified by identifying the zero-crossing location of the U_T profile (Figure 11, center), which was found at $X_{R,UT} = 39.0$ mm, as indicated by the black vertical line. This is further evaluated by analyzing the Probability Density Function (PDF) along the spanwise direction of the streamwise zero-crossing of U_T, which is presented as black curve in Figure 11 (right, top). As can be seen in this figure, the PDF covers approx. 4 mm about the peak at $X_{R,UT} = 39.0$ mm (indicated by the black vertical line), with a significant number of occurrences observed within approx. ±1 mm. In fact, the spatial standard deviation of the time-averaged reattachment location was $\sigma_{XR,UT} = 0.9$ mm.

According to these findings, the regions upstream (approx. 0 < X < 39 mm) and downstream (approx. X > 39 mm) of the critical line were identified as separated and attached flow regions, thus elucidating the change in the instantaneous wall temperature patterns described above with regard to Figure 10 (bottom) and Video-1. Interestingly, the broad minimum of the time-average wall temperature (X = 32–42 mm) extends over a streamwise range that includes also the location of zero-crossing of U_T, as shown in Figure 11 (center) and in the detail of the temperature profile presented in Figure 11 (right, bottom). In this latter figure, the red curve shows the temperature profile, which is affected by the impact of the flow-independent, fabric-like pattern described above with regard to Figure 10 (top-left). In order to identify the minimum of the time- and spanwise-averaged surface temperature, the temperature profile is approximated by a cubic function, which is shown by a blue curve. The temperature minimum was thus identified at $X_{R,T} = 38.4$ mm (as indicated by the vertical red line), i.e., close to $X_{R,UT}$. The location of wall temperature minimum therefore provides a first indication for the location of flow reattachment (as proposed in [40] for a BFS flow), but with limited accuracy due to the streamwise extent of the low-temperature region and to the influence of flow-independent thermal effects. In general, these may be induced also by a variation of the thermal properties along the surface of the investigated object (especially in the presence of wall curvature), which may lead to significant errors in the identification of the reattachment location. In contrast, the approach based on the $\vec{U}_T$ maps is only marginally exposed to non-uniform thermal boundary conditions.

The discussion of the TSB flow scenario examined in this work is largely complemented by the flowfield data reported in the next section.

Submitted to the Special Issue of *Experimental Thermal and Fluid Science* (*ETFS*) dedicated to the 6th International Conference on Experimental Fluid Mechanics (ICEFM). Revision R1

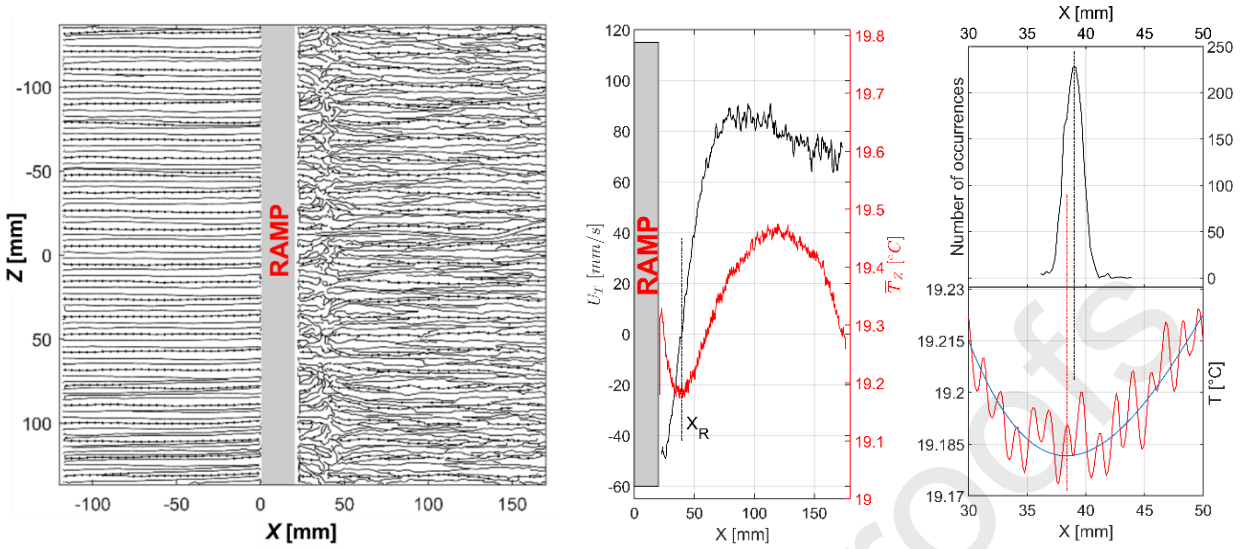

Figure 11: wall flow topology, obtained as wall streamlines of the time-averaged $\overrightarrow{U_T}$ (left), and corresponding profile of time- and spanwise-averaged U_T in the region downstream of the BFR (center). Additionally, in the center figure, the time- and spanwise-averaged wall temperature distribution is shown by a red line. The right figure shows the PDF along the spanwise direction of the streamwise zero-crossing of U_T (top) and a detail of the time- and spanwise-averaged temperature profile (red curve), with a cubic approximation function shown as blue curve. In both center and right figures, the identified reattachment location $X_{R,UT}$ is indicated by a vertical black line, while the minimum of the $\overline{T}$-profile is indicated in the right figure by a vertical red line.

5.2 Flowfield Statistics

The bin-averaging process of the LPT data gives access to highly resolved flow quantities of the examined overall statistically convergent two-dimensional flow scenario. In the following, time- and spanwise-averaged fields of velocities, accelerations, and selected Reynolds stresses will be discussed. Further results (additional Reynolds stresses and triple correlations) are reported in Appendix B.

Figure 12 illustrates the mean flow structure and velocity field, with the (main) flow from the left. The distributions of the streamwise (u) and wall-normal (v) velocity components are shown in the top and bottom figures, respectively. Additionally, the velocity streamlines are superimposed to the u-distribution in Figure 12 (top). As can be seen in this figure, the incoming TBL passes over the BFR top corner with relatively high momentum (the flow velocity is close to that of the freestream, i.e., $U_\infty = 1$ m/s for the STB measurements). The flow was observed to separate at this corner (geometry-induced separation, see Sec. 1), giving rise to a shear layer that reattaches to the surface further downstream. As expected, the fluid trapped in the TSB was observed to move upstream (negative u in Figure 12, top) and away from the wall (positive v in Figure 12, bottom). No secondary recirculation was found within the TSB, thus confirming the observations based on the $\overrightarrow{U_T}$ results (see Figure 11). This finding is also in line with the results of the preceding wind-tunnel experiments [56,57] and with previous work on 25° BFR flows [21,23–24,27,29]. A closer look at the u-distributions in the wall proximity shows that the streamwise velocity component changed its sign at $X_{R,u} = 40.8 \pm 0.2$ mm, indicating time-averaged flow reattachment at this location.

Submitted to the Special Issue of *Experimental Thermal and Fluid Science* (*ETFS*) dedicated to the 6th International Conference on Experimental Fluid Mechanics (ICEFM). Revision R1

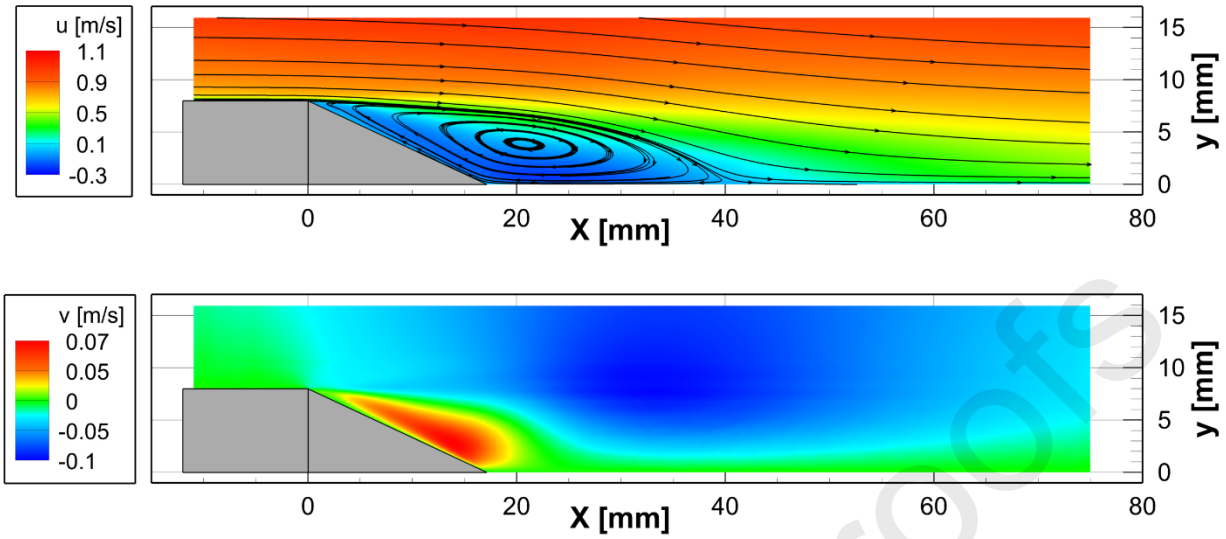

Figure 12: time- and spanwise-averaged distributions of the streamwise (top) and wall-normal (bottom) velocity components. In the top figure, streamlines based on the mean velocity vector field are also shown.

The time- and spanwise-averaged distributions of flow acceleration $\vec{a}$ are presented in Figure 13, where the top and bottom figures show the streamwise (a_x) and wall-normal (a_y) acceleration components, respectively. In both figures, streamlines from the mean velocity vector field (see Figure 12, top) are superimposed to the acceleration distributions. The streamwise distribution of a_x was found to be in agreement with the time-averaged pressure distribution measured using pressure taps and shown in Figure 9: flow acceleration was observed in the STB results for the region immediately upstream of the BFR (i.e., up to its top corner), in agreement with the local favorable pressure gradient indicated by the pressure tap measurements; the agreement holds also for the deceleration / adverse pressure gradient region at approx. 20 mm < X < 60–70 mm. Note that no pressure tap was installed along the ramp, with the closest one located at X = 20 mm; in that streamwise region (0 ≤ X < 20 mm), the streamwise acceleration of the flow in the region above the shear layer was nearly zero, while significant values of a_x and a_y were found within the TSB, as a result of the recirculation. It should be also emphasized that markedly negative values of a_y were observed in this streamwise region just above the shear layer, in agreement with the downward motion of the flow towards reattachment. Further downstream, the negative a_x-values coupled with the positive a_y-values in wall vicinity (vertical deceleration while approaching the wall) indicate a pressure maximum in accordance with the surface pressure distribution measured by the pressure taps.

Journal Pre-proofs

Submitted to the Special Issue of *Experimental Thermal and Fluid Science* (*ETFS*) dedicated to the 6th International Conference on Experimental Fluid Mechanics (ICEFM). Revision R1

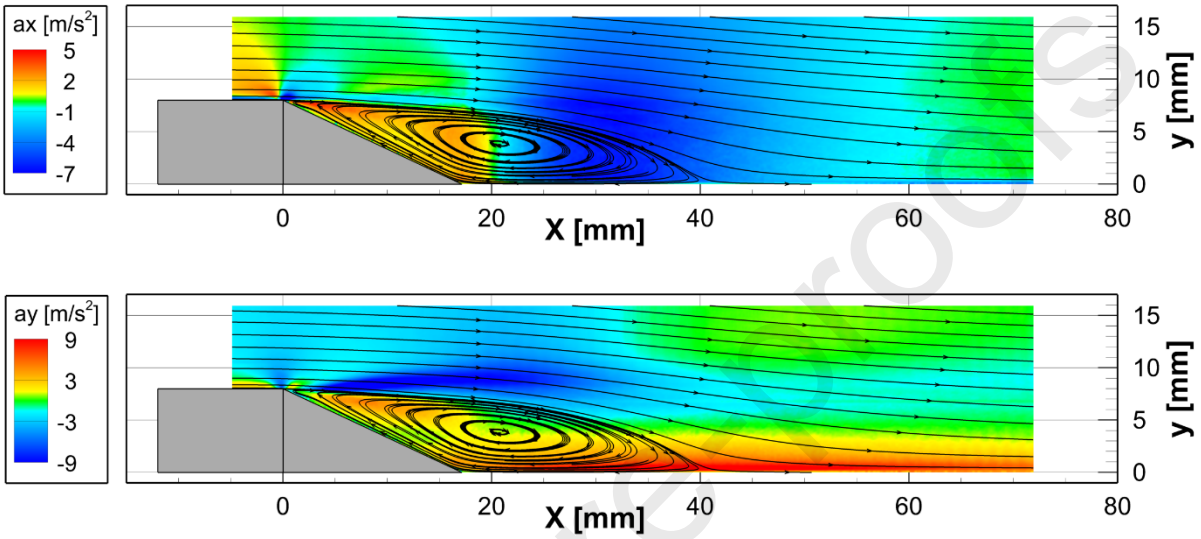

Figure 13: time- and spanwise-averaged distributions of the flow acceleration components a_x (top) and a_y (bottom), with superimposed streamlines based on the mean velocity vector field.

Time- and spanwise-averaged distributions of all six components of the Reynolds stresses were also determined from the analysis of the STB data. Figure 14 shows the results obtained for the Reynolds stresses $u'u'$ (top) and $u'v'$ (bottom). Here, u' and v' are the streamwise and wall-normal components of the fluctuating velocity, respectively. As expected, the largest values of Reynolds stresses were found along the shear layer, but significant values were still observed downstream of the time-averaged reattachment location, up to the streamwise end of the STB measurement volume. Furthermore, around $X = 20$ mm and $y = 5$ mm, the Reynolds stress distributions showed a downward-oriented bending. This appeared to occur in the region of strong variations in flow acceleration within the TSB (see Figure 13).

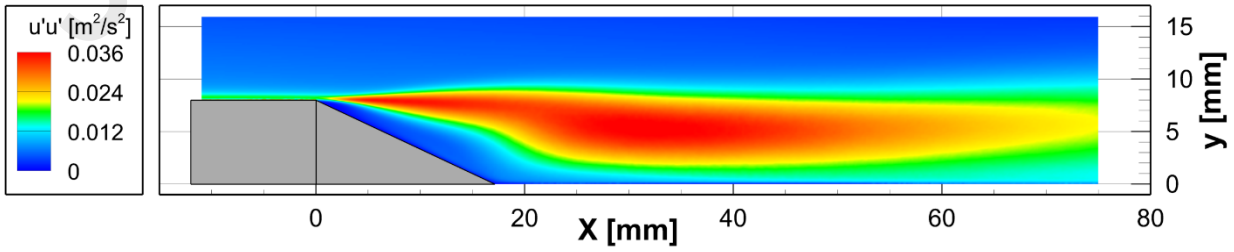

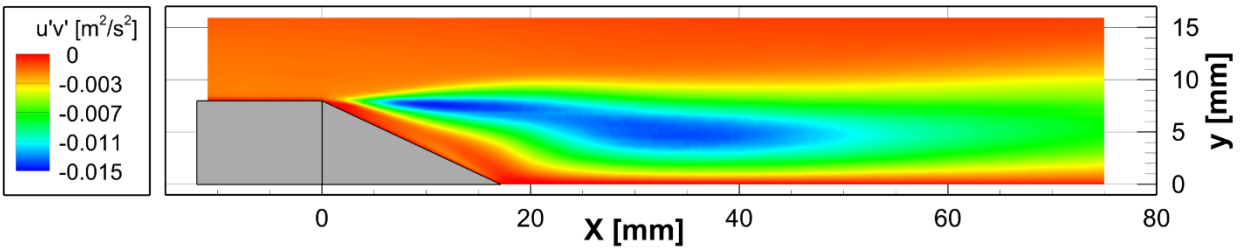

Figure 14: time- and spanwise-averaged distributions of selected Reynolds stresses: $u'u'$ (top) and $u'v'$ (bottom).

5.3 Flow Reattachment Location

Time-averaged flow reattachment downstream of the BFR was identified at $X_R \sim 5\ h$ (i.e., 40 mm) via the analysis of both TSP and STB results, which also confirmed the absence of a secondary recirculation. The reasonable, mutual agreement of the reattachment locations obtained from the evaluation of the celerity of temperature fluctuation transport (Sec. 5.1) and of the streamwise component of the velocity (Sec. 5.2) is significant, considering the differences in experimental methods (time-resolved wall temperature measurements vs. Lagrangian particle tracking), the different water-tunnel entries of the TSP and STB test campaigns (see Sec. 3), and the different modules used in the two campaigns (see Sec. 2.3). The remaining small difference in the identified time-averaged reattachment locations ($\Delta X_R = X_{R,u} - X_{R,UT} \sim 1.8$ mm) is of the same order of the sum of the reported measurement uncertainties and spanwise variations of the reattachment line (see Figure 11, top-right). As discussed in Sec. 1, the freestream turbulence is one of the flow parameters that can influence the TSB shape, size and behavior; the freestream turbulence intensity and spectral characteristics in the GWB water tunnel can depend on the freestream speed, and the slight difference in U_∞ for the TSP and STB test campaigns (see Table 1) may have had a small, but appreciable effect on the TSB extent. The TSB extent may have also been slightly influenced by the wall heat flux imposed to the TBL in the TSP measurements (see Secs. 2.3.2 and 4.1), as compared to the STB measurements with adiabatic wall: in BFS flows, homogeneous heating was reported to reduce the TSB length [6], and this may have had an influence also in the present BFR flow. In any case, it should be emphasized here that buoyancy effects due to the imposed wall heat flux, such as the mixed convection effects investigated in [97], were not present in the current study, since the temperature difference between surface and fluid was kept sufficiently small for the examined flow speed. In fact, the Richardson number in the recirculation zone was estimated to be of the order of 0.001, significantly smaller than the typically reported threshold of 0.1, above which buoyancy effects are expected to become relevant. Furthermore, an impact of the flow unsteadiness characteristic of TSBs [7,9–11], especially in the flow reattachment region, may not be excluded, which may have led to oscillations of the reattachment location and of the flow topology in its vicinity. The relationship between velocity and wall temperature fluctuations is still unexplored for non-canonical flows (see Sec. 4.1), and it may be particularly complex in the presence of the strong pressure gradients in the flow separation region (see Figure 9 and Figure 13), possibly involving different relationships for different turbulent lengthscales that should be included in the evaluation of U_T. The influence of these different aspects on the BFR flow will be investigated in future research.

The time-averaged reattachment location of $X_R \sim 5\ h$ measured in this study is in excellent agreement with that reported in previous experimental [23] and numerical work [27] on a 25° BFR, where also $X_R \sim 5\ h$ was found, in spite of the much larger BFR Reynolds number ($\mathrm{Re}_h = 92{,}000$–$246{,}000$ in [23], $\mathrm{Re}_h = 170{,}000$

in [27]). Additionally, the orientation of the flow apparatus in the experiments was also different (horizontal in [23] vs. vertical in the current work). Excellent agreement is observed also with the reattachment location obtained in the analogous experimental study of [24] for the lowest Reynolds numbers examined in that work ($X_R \sim 5.2\ h$ to $4.8\ h$ at $\mathrm{Re}_h = 30{,}000$ to $50{,}000$), while a further increase in the Reynolds number led to an appreciable reduction in the streamwise TSB extent (up to $X_R \sim 4.1\ h$ at $\mathrm{Re}_h = 70{,}000$). In further numerical studies of 25° BFR flows performed via LES at $\mathrm{Re}_h = 47{,}000$ [29] and via unsteady RANS simulations at $\mathrm{Re}_h = 123{,}000$ [21], flow reattachment was found at $X_R \sim 5.7\ h$ and $5.3\ h$, respectively. Such differences observed even among previous experimental and numerical results confirm the need of further research with joint numerical and experimental efforts to improve the understanding and prediction of TSBs in reference flow configurations. In fact, as introduced in Sec. 1 and recalled above in this section, the TSB shape, size, and behavior can be influenced by several flow parameters, such as freestream turbulence and Reynolds number. In particular, it should be noted that the turbulence levels in the wind tunnels of [23], [24], and in the GWB water tunnel are expected to be of the same order, and the inlet boundary conditions in the LES of [27] were designed to match the TBL and the freestream turbulence characteristics from [23]. In contrast, the synthetic freestream turbulence level in the LES of [29] was larger, while no detailed information is given in [29]. The comparison in the freestream turbulence level may provide an indication for the observed agreement/difference in X_R among present and previous studies, but a thorough analysis should include the consideration of further parameters that may influence the TSB characteristics, starting from the Reynolds number. The evaluation of the impact of Re_h (Re_{xh}) on the present experimental results will be the focus of future work.

5.4 Spanwise Arrangement of Flow Structures and Wall Thermal Traces

The current surface and flowfield results enable also the study of the turbulent flow structures involved in the evolution of the TBL in the presence of the BFR. In particular, the time-resolved, instantaneous temperature maps presented in Figure 10 (bottom) and in Video-1 show different patterns of wall thermal traces for the three regions at $X < 0$, $20\ \mathrm{mm} < X < 40\ \mathrm{mm}$, and $X > 40$ mm. The attached flow regions upstream of the BFR and downstream of X_R are populated by streamwise-oriented thermal traces that propagate in the streamwise direction, whereas this relatively ordered pattern appears to break down in the separated flow region.

The streamwise-oriented thermal traces resemble the streaks characteristic of attached turbulent boundary layers [98,99]. An insight into the origin of the wall thermal traces in the region downstream of the BFR is provided by the instantaneous flowfield information made available by the *FlowFit3* processing of the LPT data (see Sec. 4.2 and Appendix A.3). Examples of instantaneous, tracked particle fields are shown in Figure 15, where the reconstructed tracks are color-coded by the streamwise velocity component u. The top and bottom figures show the results obtained in wall-parallel slices within the wall-normal regions of $y = 0$–0.8 mm and 6–8 mm, respectively, thus focusing on the recirculating flow close to the wall and on the shear layer region. The corresponding videos are provided as Supplementary Material (Video-2: Slice_0-1_5mm.mp4, and Video-3: Slice_6-8mm.mp4), where it should be noted that, for illustrative purposes, the wall-normal region of the near-wall slice has been increased, as compared to Figure **15**. In the considered upper region, streamwise-oriented streaks of high/low streamwise velocity are clearly visible; they meander as the time evolves, as can be seen in Video 3. Close to the wall, the pattern turns to less elongated structures, with the appearance of flow cells encapsulated within the recirculation region followed by a rearrangement of streamwise-oriented flow structures downstream of the time-averaged reattachment location. This flow pattern close to the wall is in qualitative agreement with that observed in the time-resolved surface temperature maps. Furthermore, the streamwise-oriented streaks of high/low u observed at $y = 6$–8 mm resemble the streamwise-oriented thermal traces visible in the time-resolved temperature maps upstream of

Submitted to the Special Issue of *Experimental Thermal and Fluid Science* (*ETFS*) dedicated to the 6th International Conference on Experimental Fluid Mechanics (ICEFM). Revision R1

the BFR (see Figure 10, bottom, and Video-1), and therefore appear to originate from the interaction of the incoming TBL with the TSB shear layer.

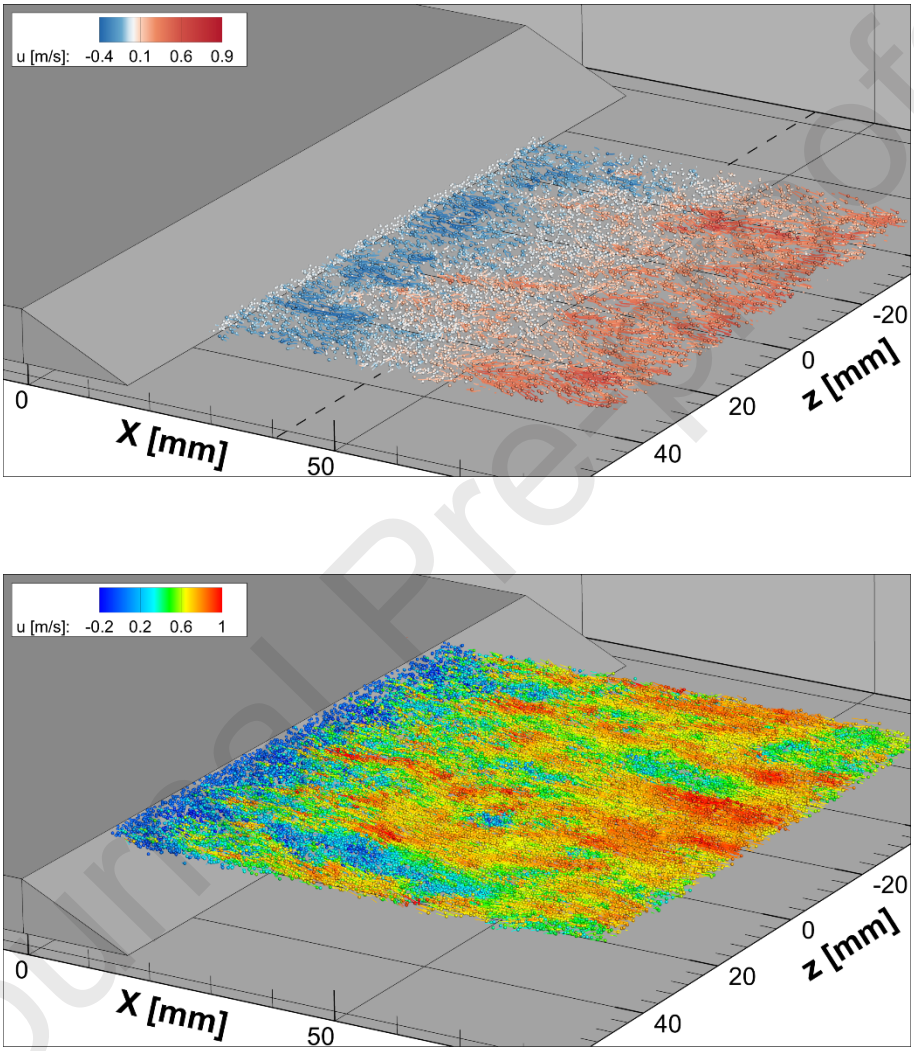

Figure 15: reconstructed particle tracks, color-coded by the streamwise velocity component u, within wall parallel slices at y = 0–0.8 mm (top) and y = 6–8 mm (bottom). Subsamples of 20 and 2 time-steps, respectively. The time-averaged reattachment location $X_{R,u}$ is indicated in the top figure by a dashed black line.

A first quantitative evaluation of the spanwise organization of these flowfield and wall thermal structures can be gleaned from both TSP and STB data by statistically focusing on the fluctuating fields of temperature and velocity, respectively. Specifically, the computation of normalized, time-averaged power spectra $\overline{P}_{\lambda}$

enables the quantification of the energy distribution of the flowfield structures at different spanwise wavelengths λ.

For T', spectra were evaluated along the spanwise direction z for the whole streamwise extent of the TSP fields, with a resolution in streamwise direction of $\Delta x_n = 0.725$ mm. Power spectra were based on Fast Fourier Transform (FFT) windows having 1,024 TSP map nodes in spanwise length (approx. 150 mm, see Sec. 4.1), resulting in a spatial frequency domain with a wavenumber resolution $\Delta\omega_\lambda = 0.0067$ mm^{-1} and a Nyquist limit at $\omega_{\lambda_{max}} = 6.897$ mm^{-1}. Following Welch periodogram approach, several FFT windows were used to cover the full signal length (1,890 nodes), with a partial overlap of 75 %.

Spectra $P_\lambda(x_n,\omega_\lambda,t_m)$ were thus evaluated at each streamwise location x_n and every time instant t_m; the final spectra $\overline{P}_\lambda(x_n,\omega_\lambda) = \frac{1}{M}\sum_{m=1}^{M} P_\lambda(x_n,\omega_\lambda,t_m)$ were obtained by time-averaging over the $M = 12{,}500$ temperature maps in time (see Appendix A.4). Spectra were normalized to contain unitary energy, forcing their intensity to be roughly comparable in a global sketch. The result of this analysis is shown in Figure **16** (center), where the obtained spectra are presented as a function of the streamwise coordinate X (horizontal axis) and of the spanwise wavenumber $1/\lambda$ (vertical axis, logarithmic). The shown black line collects the wavenumbers corresponding to the maxima of $\overline{P}_\lambda$ at each streamwise location, while the color bands indicate the spreading of the spectral values over the wavenumbers (blue to red for low to high $\overline{P}_\lambda$-values). Furthermore, a zoomed-in plot of the pressure distribution from Figure 9 is presented in Figure **16** (top) for the streamwise region corresponding to that of the TSP measurements. In both figures, the vertical dashed-dotted gray line indicates the time- and spanwise-averaged reattachment location from Sec. 5.3 ($X_R \sim 40$ mm).

In the attached flow region of nearly-zero pressure gradient upstream of the BFR, the maxima of the power spectra are found at a wavenumber of 0.05–0.06 mm^{-1}, almost invariant in the streamwise direction. This finding is in line with the qualitative observations of Figure 10 (bottom) and Video-1. The corresponding wavelength of spanwise separation between the wall thermal traces would be approx. 16–20 mm. This is in excellent agreement with the expected spanwise separation of near-wall, streamwise-oriented streaks in an attached TBL, which would be of the same order of the boundary-layer thickness ($\delta_{99} \sim 20$ mm by design at the BFR location, see Sec. 2). It should be emphasized here that a favorable pressure gradient certainly occurred upstream of the BFR, but its streamwise extent may have been shorter than the indication provided by the two pressure taps located upstream of the BFR, which were separated by a relatively large distance of $\Delta X = 2\,h$. In any case, although an impact of this localized, favorable pressure gradient on the wavenumber corresponding to the peak in $\overline{P}_\lambda$ is not observed, it appears to lead to a broadening of the power spectrum towards lower wavenumbers. The spanwise arrangement of the wall thermal traces in this region is discussed further below, after the analysis of the STB data will be presented. Immediately downstream of the BFR, the breakdown of the ordered thermal pattern described above is well quantified by the broadening of the power spectrum towards higher and lower wavenumbers, which here extends over at least an order of magnitude in ω_λ (from approx. 0.1 mm^{-1} to less than 0.01 mm^{-1}). The power spectrum characteristic of an attached boundary layer starts to be recovered at $X \sim 40$ mm, where also the streamwise distribution of the $\overline{P}_\lambda$-maxima reaches its largest value (approx. $\omega_\lambda = 0.08$ mm^{-1}). This location is highly consistent with the time- and spanwise-averaged location of flow reattachment (see Sec. 5.3). Even it is may be not surprising, this consistency is a confirmation of the validity of the present analysis. At $X > 40$ mm, the overall trend in the $\overline{P}_\lambda$-maxima shows a slight decrease towards smaller wavenumbers, recovering the wavenumber values characteristic of the maximal $\overline{P}_\lambda$ upstream of the BFR ($\omega_\lambda \sim 0.06$ mm^{-1}) around the location of local pressure minimum (approx. $X = 60$–70 mm). Downstream of this location, the further decrease is weak, with a wavenumber corresponding to the $\overline{P}_\lambda$-peak still larger than 0.04 mm^{-1} even at the downstream end of the TSP domain ($X \sim 155$ mm). Nevertheless, a shrinking of the power spectrum (with a narrower distribution about the maximum in $\overline{P}_\lambda$) can be observed when moving from $X \sim 40$ mm to $X \sim 130$ mm. The discussion of the evolution of the power spectrum in the streamwise direction as a function

of the spanwise wavenumber is continued further below, where the results of the STB data analysis are also taken into account.

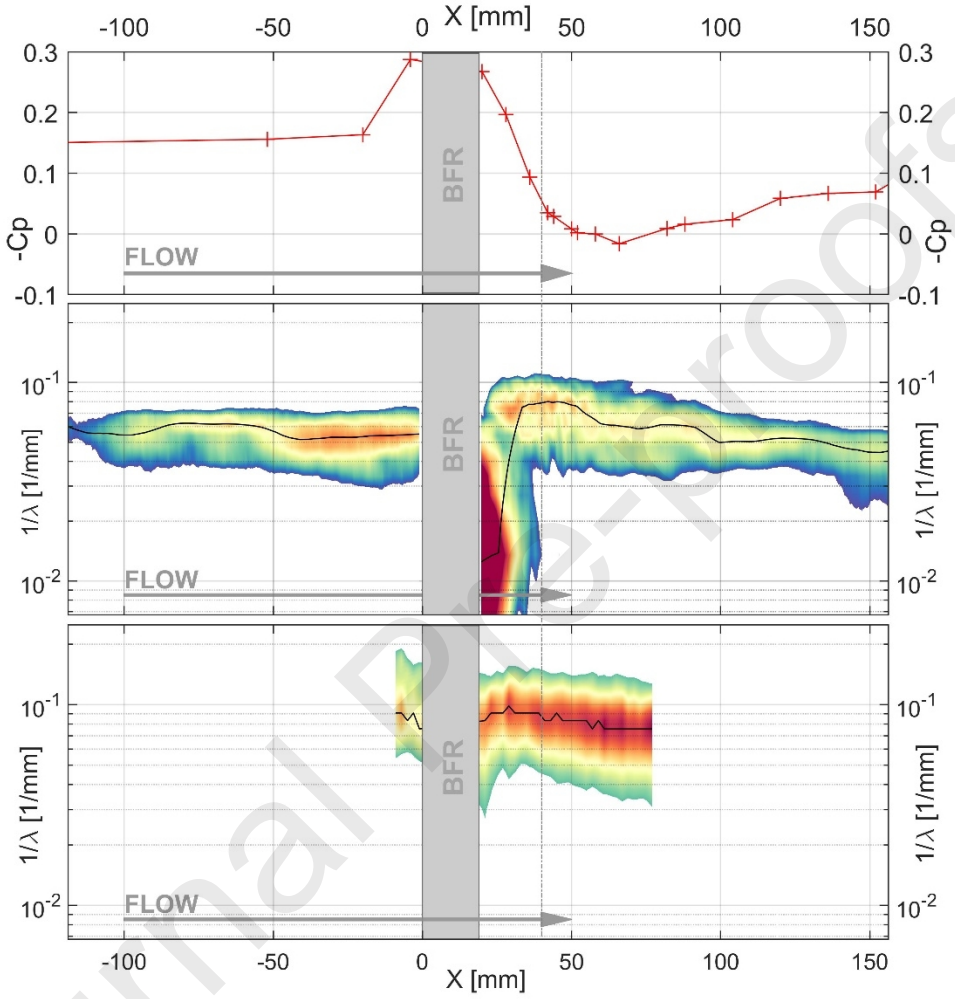

Figure 16. Top: detail of the distribution of the pressure coefficient in the region around the BFR. Center: streamwise evolution of the most energetic band of $\overline{P}_\lambda(x_n,\omega_\lambda)$ from the analysis of the TSP data, based on the temperature fluctuations maps T'. Bottom: corresponding results from the analysis of the STB data, based on the velocity correlation maps $\overline{R}_{v'v'}$. Flow is from the left. The color bands provide an indication of the spreading of the $\overline{P}_\lambda$-values over the wavenumbers (blue to red for low to high $\overline{P}_\lambda$values), with the maxima of $\overline{P}_\lambda$ shown as black lines. The vertical dashed-dotted gray line indicates the time- and spanwise-averaged flow reattachment location.

An analysis similar to that presented above with regard to the TSP data was conducted with the near-wall STB data, focusing on the wall-normal components of the velocity fluctuations v'. This choice was motivated by the expected relation of wall-normal velocity fluctuations to surface temperature fluctuations through the close link between momentum transport and wall heat flux. For this analysis, wavenumber spectra were obtained via spanwise Fourier transform of two-point (auto-)correlations, following the Wiener-Khintchine theorem [100].

The correlations were computed directly on the scattered particles employing spatial discretization. The spatial origin of the correlation was implemented as small reference box close to the wall with a streamwise × wall-normal size of 2 × 0.5 mm^2, extending for 60 mm in the spanwise direction. Any particle falling within this box was designated as a reference particle and paired with all other particles within its neighborhood as $r_i = v'_{p_i} v'_{ref} / \sigma_v$, where v'_{p_i} and v'_{ref} are the wall-normal velocity fluctuations for the i-th and reference particles, respectively, and σ_v the standard deviation of the wall-normal velocity component at the corresponding location. The particle distances $\vec{x}_{p_i} - \vec{x}_{ref} = (\Delta x, \Delta y, \Delta z)$ were discretized on a 0.2 mm grid, enabling the creation of the correlation map $R_{v'v'}(\Delta x, \Delta y, \Delta z)$ as an average over r_i in a similar binning scheme as for the flowfield statistics in Sec. 5.2. Correlation maps computed for each time-step were then time-averaged over all available data. The resulting map $\overline{R}_{v'v'}$ was analyzed via FFT in the spanwise direction, thus providing the power density spectra. In this analysis, the wavenumber resolution was $\Delta \omega_\lambda = 0.0076$ mm^{-1}, and the Nyquist limit was at $\omega_{\lambda_{max}} = 2.496$ mm^{-1}. These values are different from those of the TSP analysis because of the reduced extent and spatial resolution of the binned correlation map (661 nodes in the spanwise direction), where bins had to be chosen large enough to accumulate a sufficient number of particles for converged statistics. Separate reference boxes were placed next to each other, covering the whole streamwise extent of the STB measurement volume; accordingly, spectra were obtained at each streamwise location, with a resolution of $\Delta x_n = 2$ mm in the streamwise direction. In a manner analogous to that of the $\overline{P}_\lambda$-spectra obtained from the TSP data analysis, each spectrum was eventually normalized at the corresponding streamwise location to contain unitary energy.

The result of this analysis is presented in Figure **16** (bottom) in the same manner as for the $\overline{P}_\lambda$-spectra from the TSP data analysis (see Figure **16**, center), but obviously covering a shorter streamwise extent. Nevertheless, the availability of the results of this STB data analysis enables a quantitative comparison of the spanwise arrangement of flowfield structures and wall thermal traces. In the STB region of small streamwise extent upstream of the BFR, the maxima of the power spectra from the STB data analysis are found at wavenumbers in the range 0.07–0.09 mm^{-1}, very close to the result of the TSP data analysis for the attached flow region upstream of the BFR (see Figure **16**, center vs. bottom). Furthermore, the corresponding spectra show significant overlap in the wavenumber range 0.05 mm^{-1} < ω_λ < 0.08 mm^{-1}. (This overlap is intended in terms of absolute ω_λ-values corresponding to large $\overline{P}_\lambda$-values, rather than in terms of absolute $\overline{P}_\lambda$-values.) Downstream of the BFR, in the separated flow region, a broadening of the power spectrum towards lower wavenumbers is confirmed also in the STB results, although not as pronounced as for the TSP results. The power spectrum characteristic of an attached boundary layer starts to be recovered upstream than in the case of the wall thermal traces, with the largest wavenumber corresponding to the $\overline{P}_\lambda$-maxima reached at $X \sim 30$ mm (approx. $\omega_\lambda = 0.09$–0.10 mm^{-1}). A trend of decreasing $\overline{P}_\lambda$-maximum with increasing distance from the BFR, similar to that discussed above with regard to the wall thermal traces, is observed downstream of this location; in fact, the range of wavenumbers characteristic of the attached flow upstream of the BFR (0.07–0.09 mm^{-1}) is recovered in the region downstream of the time- and spanwise-averaged reattachment location (40 mm < X < 80 mm). This trend seems to be in line with the redeveloping attached TBL, i.e., with re-increasing boundary-layer thickness at larger X, leading to a larger spanwise distance between the near-wall flowfield structures as well as between the related wall thermal traces. Nevertheless, the local streamwise pressure gradient (adverse up to $X \sim$ 60–70 mm, favorable further downstream) may also influence this spanwise arrangement. A local change in boundary-layer thickness and streamwise pressure gradient may have also had an impact on the arrangement of the flowfield structures immediately upstream of the BFR, since a decrease in characteristic wavenumbers may be inferred from the result of the STB data analysis (see Figure **16**, center). However, the wall thermal traces do not show this trend, and the limited extent of this region in the STB measurement volume does not allow a more detailed trend evaluation.

At $X = 40$ mm, the wavenumber corresponding to the maximum $\overline{P}_\lambda$ is found at $\omega_\lambda = 0.08$–0.09 mm^{-1} in excellent agreement with that for the wall thermal traces (approx. $\omega_\lambda = 0.08$ mm^{-1}). With increasing

streamwise distance from the reattachment location, the wavenumbers corresponding to the maximal $\overline{P}_\lambda$ show slight differences, while remaining close: for example, at $X = 70$ mm, they are found at $\omega_\lambda = 0.07$–0.08 mm^{-1} and at approx. $\omega_\lambda = 0.06$ mm^{-1} in the STB and TSP results, respectively. At the same time, the power spectra from the STB data analysis appear to broaden towards lower and higher wavenumbers, a trend opposite to that observed for the wall thermal traces. Nevertheless, also significant overlap of the power spectra obtained from the STB and TSP data analysis is found in the region downstream of the BFR: for example, at $X = 40$ mm and 70 mm the overlap extends over the wavenumbers 0.05 mm$^{-1} \leq \omega_\lambda \leq 0.10$ mm^{-1} and 0.04 mm$^{-1} \leq \omega_\lambda \leq 0.09$ mm^{-1}, respectively.

Summarizing the findings of this spectral analysis, consistent results are observed, in general, for the wavenumbers characteristic of the spanwise arrangement of the near-wall flowfield structures and of the wall thermal traces. In quantitative terms, the agreement of the wavenumbers corresponding to the maxima in the power spectra is reasonable for both regions upstream and downstream of the BFR, and in some portions of these areas the agreement is even excellent. Furthermore, the trends of slightly decreasing characteristic wavenumbers with increasing streamwise distance downstream of the time- and spanwise-averaged reattachment location are consistent. In qualitative terms, a broadening of the power spectra towards lower wavenumbers is observed in both STB and TSP results for the separated flow regions. These generally consistent results provide an encouraging indication of the relationship between the observed flowfield structures and wall thermal traces. Especially in the attached flow regions, it may be reasonably inferred that the streamwise-oriented thermal pattern is the wall signature of the elongated streaks in the boundary layer evolving along the surface, resulting from the close relationship between momentum and thermal transfer. The comparison, however, also poses new questions regarding the thermal reaction at the wall to the impact of flowfield changes, such as those induced, for example, by pressure gradient variations. It may be conjectured that the reaction of the turbulent flow structures to such changes is faster than the corresponding thermal transfer to the surface, thus leading to, e.g., a spatial lag in the streamwise evolution of the spanwise spectral characteristics. At the same time, as discussed in Sec. 5.3, the relationship between velocity and wall temperature fluctuations may also involve a dependency from the turbulent lengthscales. These relations would deserve further research in future work; in particular, experimental investigations should be ideally performed via simultaneous TSP and STB measurements to ensure that the turbulent flow structures are captured at exactly the same place and time.

6 Conclusions

Flow separation and reattachment of a turbulent boundary layer, as induced by a 25° backward-facing ramp, were experimentally investigated in this work using advanced optical measurement techniques: temperature-sensitive paint and dense 3D Lagrangian particle tracking by Shake-The-Box. The experiments were performed in the Large Water Tunnel of TU Braunschweig on a quasi-two-dimensional (i.e., spanwise-invariant), symmetric flat-plate model featuring a nearly-zero streamwise pressure gradient. A tripping device was applied in the leading-edge region to force laminar-turbulent transition, thus ensuring that a fully developed turbulent boundary layer was investigated and enhancing flow symmetry. The examined Reynolds numbers, based on the ramp height and streamwise ramp position with respect to the plate leading edge, were 8,800 and $1.2 \cdot 10^6$, respectively. The modular model design enabled the installation of three different, exchangeable modules that comprised also the backward-facing ramp: a pressure module equipped with pressure taps upstream and downstream of the ramp; a TSP module with a europium-based TSP applied on laminate layups upstream and downstream of the ramp; and an STB module with an embedded glass insert. A current-carrying carbon fiber layer was integrated into the TSP laminates to impose a wall heat flux and thus enhance the flow-induced thermal signatures on the surface, whereas the

glass insert of the STB module was designed to avoid wall reflection of the illumination light for the STB measurements. Additionally, the main body of the flat-plate model was also equipped with pressure taps. The experiments were carried out in three successive test campaigns: in the first test campaign, the streamwise, time-averaged surface pressure distribution was measured by means of the pressure taps. These measurements showed that a nearly-zero pressure gradient was attained on a significant portion of the flat plate, while the ramp induced adverse and favorable pressure gradients in its vicinity. In the second test campaign, the TSP measurements provided time-resolved surface temperature distributions upstream and downstream of the ramp; they showed essentially two-dimensional time-averaged temperature fields populated by wall thermal traces evolving in space and time. These results were obtained after dedicated processing of the TSP images, which required spatial and temporal filtering steps that included the removal of a temporal drift and of temporally localized spikes in the TSP signal (likely originating from the LEDs used for TSP excitation). In the third test campaign, Lagrangian tracks of polyamide particles were obtained upstream, over, and downstream of the ramp via STB employing a two-stage scanning process, which enabled the attainment of high particle concentration in two subvolumes (a lower one closer to the wall downstream of the ramp and an upper one comprising the outer boundary-layer region), while at the same time limiting the imaged particle density. The STB data in the lower subvolume were processed via variable time-step STB to determine also the tracks of the slowly moving particles in the recirculation region, while avoiding false reconstructions and bias in the track positions; in contrast, standard STB processing was conducted for the upper subvolume.

The TSP and LPT data were further evaluated to obtain the distributions of flow quantities relevant for the study of the ramp-induced turbulent separation bubble. The time-resolved surface temperature distributions were analyzed to determine the time-averaged map of the celerity of propagation of temperature perturbations ($\vec{U}_T$), which was obtained by minimizing the difference between the experimentally observed behavior of the wall temperature fluctuations and that predicted by the Taylor hypothesis of "frozen turbulence". Relying on the relationship between $\vec{U}_T$ and the friction celerity and on the obtained wall flow topology, flow reattachment was identified at the locations of convergence of the $\vec{U}_T$ wall streamlines, i.e., at the streamwise location of zero-crossing of the streamwise component of $\vec{U}_T$ for each spanwise location. Bin-averaging of the Lagrangian particle tracks provided time- and spanwise-averaged distributions of flow velocity, acceleration, Reynolds stresses and triple correlations. Furthermore, instantaneous flowfield snapshots were obtained via Navier-Stokes regularized interpolation and data assimilation. The flowfield statistics enabled: the identification of the time- and spanwise-averaged location of flow reattachment (at the location of zero streamwise velocity close to the wall); the evaluation of the flow acceleration components around and downstream of the ramp, which were found to be in accordance with the surface pressure distributions; and the identification of the largest values of Reynolds stresses along the shear layer and of their still significant magnitudes downstream of flow reattachment.

The time-averaged reattachment locations identified in the distributions of the flow velocity and of the celerity of propagation of temperature perturbations were observed to be in reasonable, mutual agreement. This is a notable result, especially when considering that the measurements were not performed simultaneously and that the identification methods are based on different quantities. The minimum of the streamwise distribution of the time-average surface temperature was also found to provide an indication for the location of flow reattachment; in general, however, this criterion may be misleading in cases affected by flow-independent thermal effects, while the celerity-based criterion enables an identification of critical lines even in such cases.

Time-averaged flow reattachment was identified in the present work at a streamwise distance from the ramp top corner corresponding to approximately 5 ramp heights. Furthermore, no secondary flow recirculation was observed for the examined backward-facing ramp: neither in the celerity field nor in the flowfield statistics. These results (time-averaged reattachment location and absence of secondary recirculation) were in agreement with those reported in previous numerical and experimental work on 25° backward-facing ramps with similar freestream turbulence characteristics, in spite of differences in ramp-based Reynolds numbers and, in the case of the experimental studies, in the examined experimental configurations.

The instantaneous, three-dimensional flowfields and the instantaneous surface temperature fields enabled capturing turbulent flow structures and their thermal signatures at the surface, which arrangement and temporal evolution strongly varied depending on the examined flow region. In the attached flow region upstream of the ramp, streamwise-oriented wall thermal traces were observed, resembling the thermal signature of the streamwise-oriented streaks of high/low streamwise velocity characteristic of attached turbulent boundary layers. Downstream of the ramp top corner, streamwise-oriented streaks of high/low u were found in the shear layer region, whereas close to the wall – i.e., in the recirculation region – the turbulent flow structures were observed to break down into smaller scales. This behavior was in agreement with that of the wall thermal traces, which showed upstream displacement and the appearance of smaller, time-varying cells. From the region around the time-averaged reattachment location, an arrangement of the turbulent flow structures and of their thermal signature similar to that observed upstream of the ramp started to be recovered, and a streamwise-oriented, streaky pattern was found also for the attached turbulent boundary layer further downstream. A quantitative evaluation of this spanwise organization of the wall thermal traces and of the near-wall flowfield structures was enabled by a spectral analysis of the fluctuating fields of wall temperature and velocity. The energy distribution of the wall thermal and flowfield structures at different spanwise wavenumbers was obtained via Fourier transforms in the spanwise direction of the maps of wall temperature fluctuations and of two-point correlations of wall-normal velocity fluctuations; this allowed an evaluation of the streamwise evolution of the characteristic wavenumbers for the whole streamwise extent of the TSP and STB measurement regions. In the region of nearly-zero pressure gradient upstream of the ramp, the maxima of the power spectra of the wall temperature fluctuations were found in a small range of wavenumbers, which was almost invariant in the streamwise direction and was in line with the expectations for an attached TBL (based on the boundary-layer thickness). In the separated flow region immediately downstream of the ramp, the power spectra from both TSP and STB data analysis were observed to broaden over a wider range of wavenumbers, while a spectral distribution characteristic of an attached boundary layer started to be recovered around the time- and spanwise-averaged reattachment location. Further downstream, the spanwise wavenumbers corresponding to the maxima in the power spectra were found to slightly decrease in the streamwise direction. These consistent, qualitative trends in the TSP and STB results were corroborated by reasonable, in some areas even excellent agreement of the values of these characteristic wavenumbers.

The achieved measurement resolution of the three-dimensional flowfield and two-dimensional surface temperature field has not been available yet for a turbulent boundary layer undergoing geometry-induced separation and subsequent reattachment, since experimental data in the flowfield have been measured mainly in profiles and planes, and quantitative surface information have been obtained so far only at discrete locations. Furthermore, the time-averaged distributions of flow acceleration and temperature fluctuation celerity are novel for this research topic. The former provide a flowfield description complementary to the wall pressure distribution that is usually unattainable for flow measurement techniques. The latter enable a quantification of the spanwise distribution of the time-averaged location of flow reattachment, which is crucial not only for the experimental analysis of the examined flow reference configuration, but also for the

validation and further improvement of RANS turbulence models, especially when two-dimensional flow is assumed at reattachment for a (quasi-) two-dimensional configuration. Similarly, the described evolution of the three-dimensional flow structures and of the related thermal traces at the wall, with the quantification of their characteristic spanwise arrangement, is not only valuable for an advancement in the physical understanding of turbulent boundary layers undergoing separation and reattachment, but also for the assessment of the spectral separation between flow features and turbulence, which is typically assumed in RANS modeling. Finally, the accurate, highly resolved fields of mean velocity (which provide also accurate information on the mean streamline curvature) and Reynolds stresses would support reliable validation of RANS turbulence models as well as their extension in near-wall flows and in flows with strong shear; in particular, Reynolds stress transport models may be improved via a flow-feature adapted change of the Reynolds stress anisotropy, based on the present experimental data.

The obtained experimental dataset is available for collaborative purposes upon request.

Acknowledgements

This work was conducted within the framework of the DLR *ADaMant* Project. The German Federal Ministry for Economic Affairs and Energy is gratefully acknowledged for its financial support. The authors would also like to thank: A. Bo, T. Hermann, K. Kienass, and T. Kleindienst (DLR Institute of Aerodynamics and Flow Technology) as well as C. Fuchs (DLR Systemhaus Technik) for the support to the installation of the experimental setup and to the conduction the measurement campaign; U. Henne (DLR Institute of Aerodynamics and Flow Technology) for the assistance in the data acquisition and storage; V. Ondruš (FH Münster) for the chemical development and synthesis of the used temperature-sensitive paint; H. Fink, B. Lange, V. Len, M. Tang, and M. Tegeler (DLR Systemhaus Technik) for the engineering of the model, of its mechanical support, of the optical access, and of the heating system; J. Breustedt, D. Drößler, B. Eilerts, D. Fengewisch, M. Göhler, E. Hasse, M. Kube, M. Moser, L. Rehbein, L. Rettberg, M. Reuter, N. Schmidt, S. Sieberts, J. Ulbrich and H. Wicharz (DLR Systemhaus Technik) for model manufacturing and installation as well as for the model instrumentation with conventional sensors; M. Brinsa (DLR Systemhaus Technik) for the organizational assistance to these experimental activities; and M. Hilfer, P. Scholz, and D. Rival (TU Braunschweig) for the practical and organizational support to the measurements in the GWB water tunnel.

Declaration of competing interests

The authors have no competing interests to declare that are relevant to the content of this article.

Funding sources

This research received no external funding.

Journal Pre-proofs

Declaration of generative AI in scientific writing

Generative AI was not used in this article.

Author contributions

Conceptualization: MC, AS, TK, and CG; Data curation: MC, DS, and MM; Formal analysis: MC, ADV, PG, DS, AS, and MM; Funding acquisition: CG; Investigation: MC, ADV, RG, JL, DS, AS, StS, and MM; Methodology: MC, CK, RG, PG, DS, AS, TK, CG, and MM; Project administration: MC, AS, CG, and StS; Resources: CK, RG, AS, CG, and StS; Software: MC, ADV, PG, DS, StS, and MM; Supervision: CK, AS, and CG; Validation: MC, ADV, DS, and MM; Visualization: MC, ADV, JL, DS, and MM; Writing – original draft: MC, ADV, DS, AS, CG, and MM; Writing – review and editing: MC, JL, PG, DS, AS, and MM.

Journal Pre-proofs

Submitted to the Special Issue of *Experimental Thermal and Fluid Science* (*ETFS*) dedicated to the 6th International Conference on Experimental Fluid Mechanics (ICEFM). Revision R1

Appendix

A Details on the Experimental Setup, Data Acquisition and Processing

A.1 Flat-Plate Model

As introduced in Sec. 2.2, the flat-plate model comprised a main body and a module, which can be exchanged among three options: a pressure module, a TSP module, and an STB module. This is illustrated by the sketch shown in Figure 17.

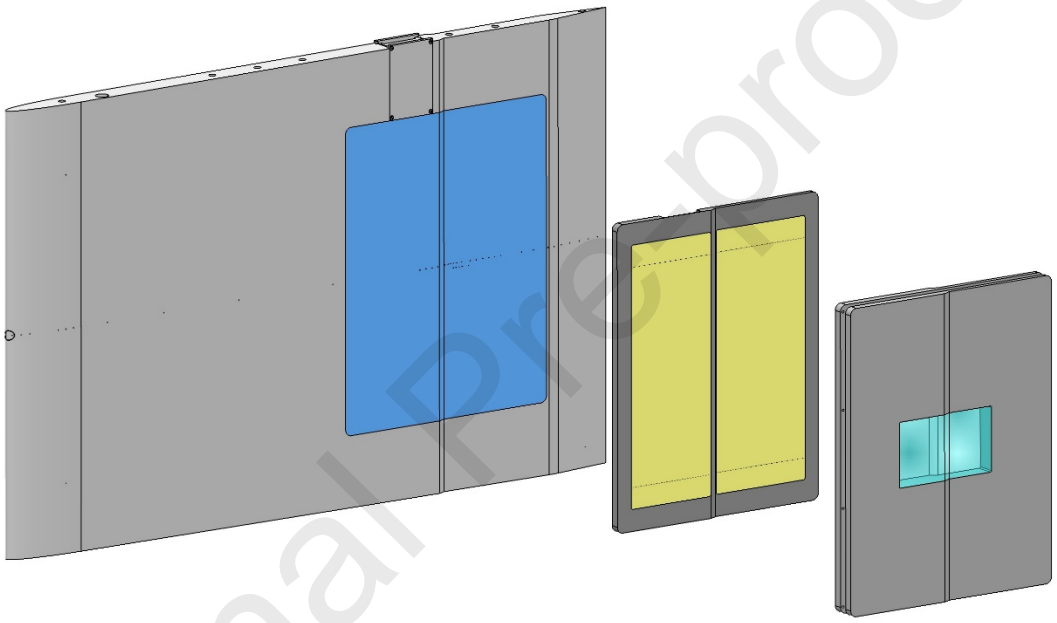

Figure 17: schematic of flat-plate model with the three exchangeable modules: pressure module (installed in the model), TSP module (center) and STB module (right).

This section of the Appendix also provides further details on the TSP module. It was composed of two laminates, manufactured of fiber-reinforced plastic, embedded into an aluminum frame. The layup of the laminates is sketched in Figure 18 and described below from the top to the bottom layer, as seen from the model surface. The application of the different layers also followed this order.

The laminates were manufactured in two separate negative molds made of aluminum, on which a release agent was applied after accurate surface polishing. The following description holds for both laminates. The TSP active layer (with a thickness of approximately 40 µm) was applied directly to the surface of the cured release agent. The active layer consisted of a europium complex (luminophore) incorporated into a commercial polyurethane clear-coat binder [81]. The luminophore is excited in the wavelength range λ_{ex} = 350–450 nm, and it emits in the wavelength range λ_{em} = 600–630 nm. The luminescent lifetime of the used TSP is of the order of 200–300 µs for the temperature range of the present experiment. A white screen layer of 200 µm thickness, which acts as thermal and electrical insulator and also functions as a diffusive

light-scattering background, was applied onto the TSP active layer. A thin layer (80 μm) of Glass-Fiber-Reinforced Plastic (GFRP) was placed onto the screen layer in order to guarantee additional electrical insulation. The CFRP layer, with a thickness of 100 μm, was then applied. It was connected to two copper-based contacting strips of 50 mm width, which were placed at the spanwise ends of the CFRP layer and oriented in the streamwise direction, as sketched by the brown strips in Figure 3 (left). The CFRP layer was thus connected through two wires to the external power supply for the electrical heating system. The electrical voltage acting on the CFRP layer was monitored via two additional wires connected to the contacting strips. The electrical resistance of the CFRP layers was 1.46 and 1.32 Ω for the upstream and downstream laminates, respectively. The further three, thicker layers composing the TSP laminates (two GFRP layers and a polymethacrylimide foam layer, PMI) served as main thermal insulation. The total thickness of the laminates was 16.2 mm. Note that, since the TSP active layer was applied to the polished negative mold, the TSP surface quality after demolding was already very good, without the need of additional polishing: the average roughness value was $R_a = 0.03$ μm, with a mean roughness depth $R_z = 0.22$ μm. These roughness values were measured by means of a contact profilometer with a vertical resolution of ±0.8 nm. In the photograph of the TSP module shown in Figure 3 (right), black markers with circular shape can be also seen in the TSP fields. They were used for TSP image processing, as described in Appendix A.4. The markers were applied on the (bottom) surface of the TSP active layers before application of the screen layers; therefore, they were not exposed to the flow. The TSP module was also equipped with 4 thermocouples (type K, wire diameter 0.08 mm, accuracy of ±0.3 K) to monitor the laminate temperature below the TSP active layer. The thermocouples were arranged along the centerline, with two thermocouples mounted into each laminate.

As shown in Figure 3 (left), the span width (lateral extent) of the TSP laminates was 600 mm, being the effective TSP surfaces 500 mm wide (because of the contacting strips at their spanwise ends). The streamwise extents of the TSP fields upstream and downstream of the BFR were 212 and 238 mm, respectively.

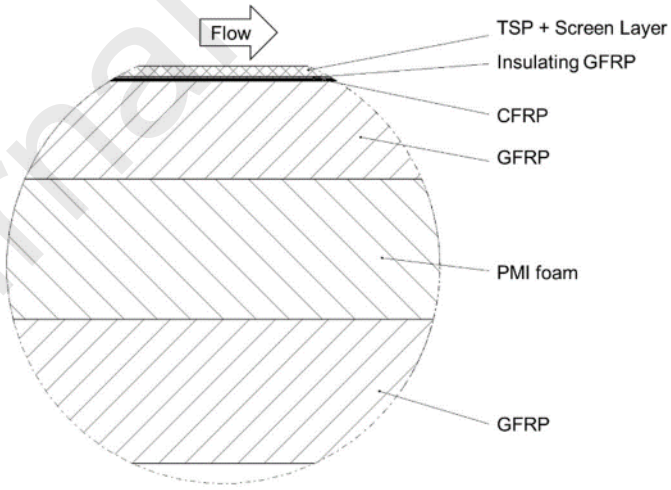

Figure 18: sketch of the layup of the laminates manufactured for the TSP module.

A.2 Optical Access

The schematic presented in Figure 19 shows the flat-plate model mounted in the GWB test section and the optical access specifically designed for the current experiment. Note that, in this figure, the STB module is

installed in the model. Furthermore, some panels of the GWB test section have been removed in Figure 19 to facilitate the visualization. The optical access panel featured 8 circular windows; 5 of these 8 windows had a diameter of 100 mm and were aligned vertically, with their center placed at the same streamwise location as that of the BFR (i.e., at x_{WT} = 3.25 m). The central window surface was parallel to the side wall, while the other four windows were tilted by an angle of 18.8° (for the two windows closer to the centerline) and 34.2° (for the farther windows) with respect to the side wall. This arrangement was optimized for the particle imaging in the STB measurements, as discussed in Sec. 2.3.3. Two of the remaining windows were placed downstream of this main set of windows and had a diameter of 75 mm; the last window, placed upstream of the main set of windows, had a diameter of 67 mm. These three windows were used for excitation of the TSP through LEDs, as shown in Figure 4. The surfaces of these three windows were parallel to the side wall. The GWB top and bottom walls were also equipped with circular windows (140 mm diameter) placed around the BFR location, as shown in Figure 19. These windows were used for laser illumination in the STB measurements (see Sec. 2.3.3).

All metallic components of the side-, top-, and bottom-wall panels, as well as the flat-plate model (exchangeable modules included) were made of aluminum; their surfaces were black-anodized to increase their resistance against corrosion and to reduce their influence on the optical measurements due to light reflections. The remaining panels of the GWB test section were made of stainless steel.

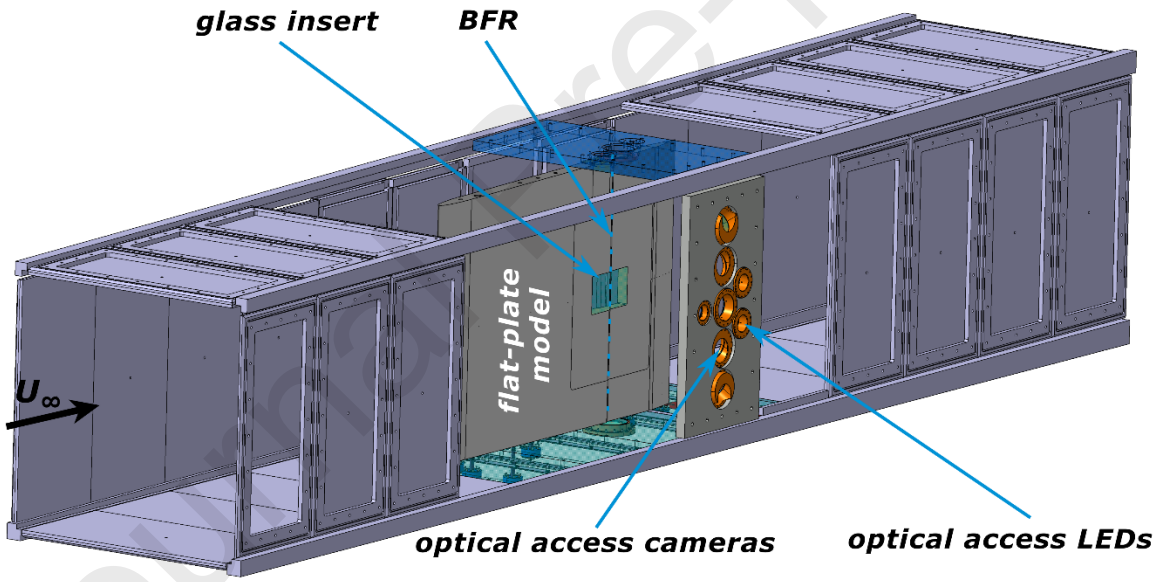

Figure 19: schematic of model installation in GWB (here: with STB module installed). The side-wall panel with the window inserts for optical access (circular orange flanges) as well as the top- and bottom-wall panels with the window for laser illumination are also depicted. Some panels of the GWB test section have been removed to facilitate the visualization.

A.3 STB Measurement System and Data Processing

In order to prevent sticking and clustering of the polyamide particles (see Sec. 2.3.3), a small amount of isopropanol was mixed with the tracers along with distilled water. This particle solution, achieved by means of electromagnetic stirring over several minutes, was supplied into the water tunnel to provide the necessary

seeding. The Stokes number of the particles was proven to be below 0.001 for the examined test conditions, thus guaranteeing accuracy in the flow tracing.

The STB method is capable to perform tracking even at high particle image densities, but the accuracy in the determination of the particle position declines for higher particle image densities due to particle image overlap. This is especially the case with laser-based illumination, since light scattered on particles being imaged in close neighborhood is likely to cause interference effects. By always illuminating only one half of the volume, these effects were attenuated in the present work while maintaining the full measurement resolution, as the particle number in the volume did not change. Such high particle concentration in the volume was achieved via the used dual-head laser (see Sec. 2.3.3), which has an excellent pulse-to-pulse stability. This guaranteed consistent illumination quality with a root-mean-square of the fluctuations of less than 1 % of the illumination intensity.

As introduced in Sec. 4.2, the STB data processing for the lower subvolume was carried out via VT-STB [45]. This extension to the standard STB data processing is beneficial in cases with a broad range of flow velocities, such as in the examined lower subvolume, which comprises a recirculating flow region, the shear layer, and part of the outer boundary layer. In fact, slowly moving particles are more likely to lead to coherent false reconstructions (also known as *ghost particles*) when standard tracking algorithms are used, since they do not move significantly between frames. Additionally, overlaps of particle images that are sustained over multiple time-steps can bias the track position, thus leading to increased noise and terminated tracks due to prediction errors. The VT-STB processing applies several passes of STB, going forwards and backwards in time, while successively increasing the temporal resolution.

For the analysis of the lower subvolume, which was characterized by strong differences in average velocities due to recirculating flow, four VT-STB passes were applied; they had the following properties: 5_f, 2_b, 1_f, and 1_b, where the numbers correspond to the multiple of the used time-step (*dt*), and the subscripts indicates the direction in time (*f*: forwards vs. *b*: backwards). The larger temporal separation of the first pass (5 *dt*) allowed the accurate tracking of the slowly moving particles close to the wall, as well as of the particles sticking to it (in total up to about 3,000, among which a few hundred sticked to the model surface). The high positional accuracy combined with this number of particles allowed a correction in relative vibrations (due to vibrations of model and/or optical setup) of the order of 1 μm, as accomplished by averaging the positional shift of the surface-sticking particles. The second pass (2_b) permitted the tracking of the low-acceleration particles (about 70,000 particles). Finally, the last two passes (1_f and 1_b) enabled the tracking of the particles in accelerated flow regions, while at the same time reconnecting partial tracks from the preceding passes. In total, about 120,000 particles were tracked in the lower subvolume after the last pass.

For the upper subvolume, standard STB processing, consisting of two passes of (1_f, 1_f), was performed, since this flow region was largely dominated by the TSB shear layer and by the outer boundary layer. About 145,000 and 160,000 particles were tracked within this subvolume in the first and second passes, respectively.

Examples of the STB results achieved after temporal fitting of the obtained particle tracks (via *TrackFit*) and Navier-Stokes regularized interpolation and data assimilation (via *FlowFit3*) are shown in Figure 20 for the whole measurement volume, where snapshots of tracked particles and Q-criterion iso-surfaces (with $Q = 10^4$ s^{-2}) are presented in the left and right figures, respectively. In both figures, the streamwise velocity component *u* is used for color-coding. The corresponding videos (Video-4: TrackedParticles.mp4, and

Video-5: Q10000.mp4) show the temporal evolution of the tracked particles and of the Q-criterion iso-surfaces, respectively.

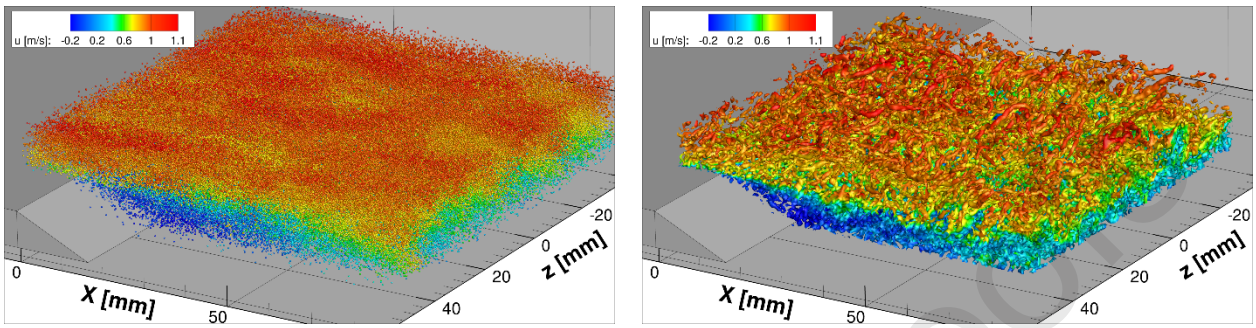

Figure 20: snapshots of tracked particles (left) and iso-surfaces with Q-criterion of 10^4 s^{-2} (right) for the whole STB measurement volume. Both the tracked particles in the left figure and the iso-surfaces in the right figure are color-coded by the streamwise velocity component *u*.

A.4 TSP Data Acquisition and Processing

The TSP image acquisition procedure consisted of:

- a *Ref* phase, in which a set of 500 TSP images was acquired at quiescent conditions and with inactive heating system;
- and a *Run* phase, in which a set of 12,500 TSP images was acquired with running tunnel and activated heating systems.

The *Run* image acquisition was started after the desired flow speed had been attained, the flow conditions had become stable, and quasi-stationary thermal conditions of the TSP laminate upper layers had been reached. This latter requirement was met by monitoring the temperatures measured by the four thermocouples installed in the TSP laminates (see Sec. 2.3.2).

Time-resolved surface temperature maps were obtained from the *Run* TSP images relying on the reference images (*Ref* phase) and a known relation between the temperature and the acquired TSP luminescent intensity (calibration function). In the *Ref* set of images, the model surface temperature was reasonably assumed to be uniform and stationary; it was taken as equal to the fluid temperature. The first step of the TSP image processing was the averaging of the *Ref* TSP images to improve the signal-to-noise ratio. As the next step, the *Run* TSP images were divided by the average *Ref* image. Note that no alignment of *Ref* and *Run* TSP images was performed, since vibrations of the experimental setup (model and optical setup) were very small (see Appendix A.3) and were found to have negligible impact on the TSP image processing. The divided TSP images were then projected (orthorectified) into the metric three-dimensional Euclidean space by using the black circular markers applied below the TSP active layer (see Sec. 2.3.2). A description for the used orthorectification procedure is provided in [51]. Finally, the surface temperature distributions were evaluated quantitatively by applying the calibration function to the resulting data. The calibration function between the TSP intensity ratio and the surface temperature was determined experimentally in [63] by investigating a TSP sample in a calibration system, in which the variation of the luminescent intensity was

determined for a series of accurately set temperatures covering the range examined in the current experiment.

B Additional Results

Distributions of additional components of the time- and spanwise-averaged Reynolds stresses obtained from the analysis of the STB data are shown in Figure 21: $v'v'$ (top) and $w'w'$ (bottom), where w' is spanwise component of the fluctuating velocity. The observations on the maximal Reynolds stress values and on the downward-oriented bending around $X = 20$ mm and $y = 5$ mm, as reported in Sec. 5.2 (Figure 14) with regard to $u'u'$ and $u'v'$, hold also for the present Reynolds stress components.

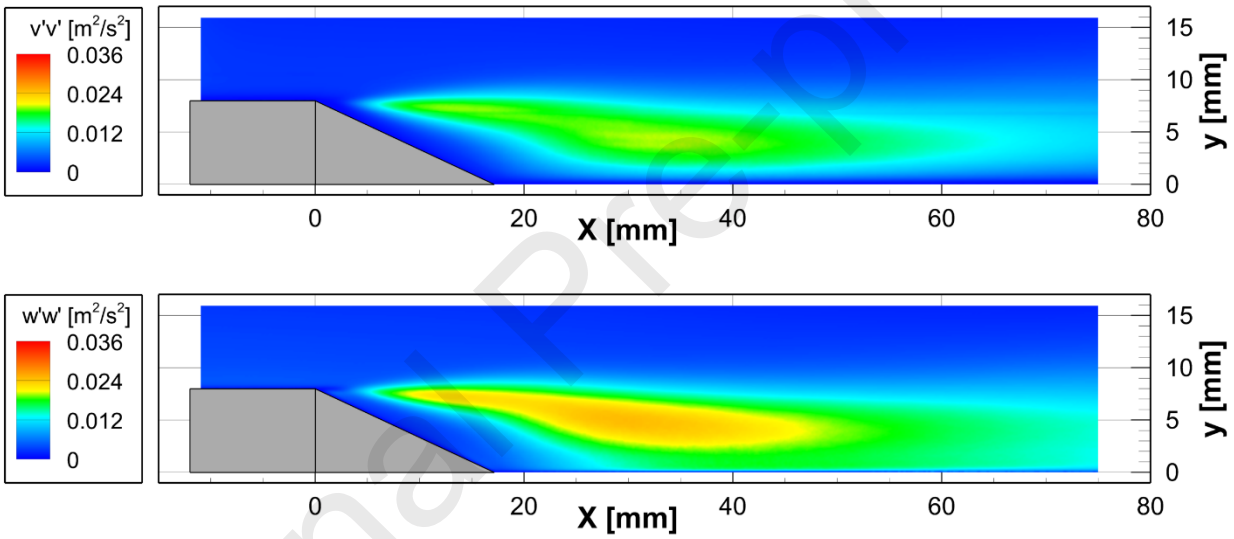

Figure 21: additional time- and spanwise-averaged distributions of Reynolds stresses: $v'v'$ (top) and $w'w'$ (bottom).

Finally, the available LPT data allowed an evaluation of statistically converged distributions of triple correlations, which represent the transport of Reynolds stresses by turbulent velocity fluctuations and hence are central to the energy transfer from large to small turbulent scales. Two examples of triple correlation distributions ($u'u'v'$ and $v'v'u'$) are reported in Figure 22 (top and bottom, respectively). Regions with large absolute values of these triple correlations were observed to extend significantly downstream of the BFR, as induced by the impact of a strong u' component (see also Figure 14, top). It should be also noted that the triple correlations change sign in the wall-normal direction; their zero-crossing lines are in reasonable agreement with the distributions of the Reynolds stress maxima shown in Figure 14 and Figure 21. Analogously, the distributions of positive triple correlations showed a downstream-oriented bending, similar to that of the Reynolds stresses close to the wall.

Submitted to the Special Issue of *Experimental Thermal and Fluid Science* (*ETFS*) dedicated to the 6th International Conference on Experimental Fluid Mechanics (ICEFM). Revision R1

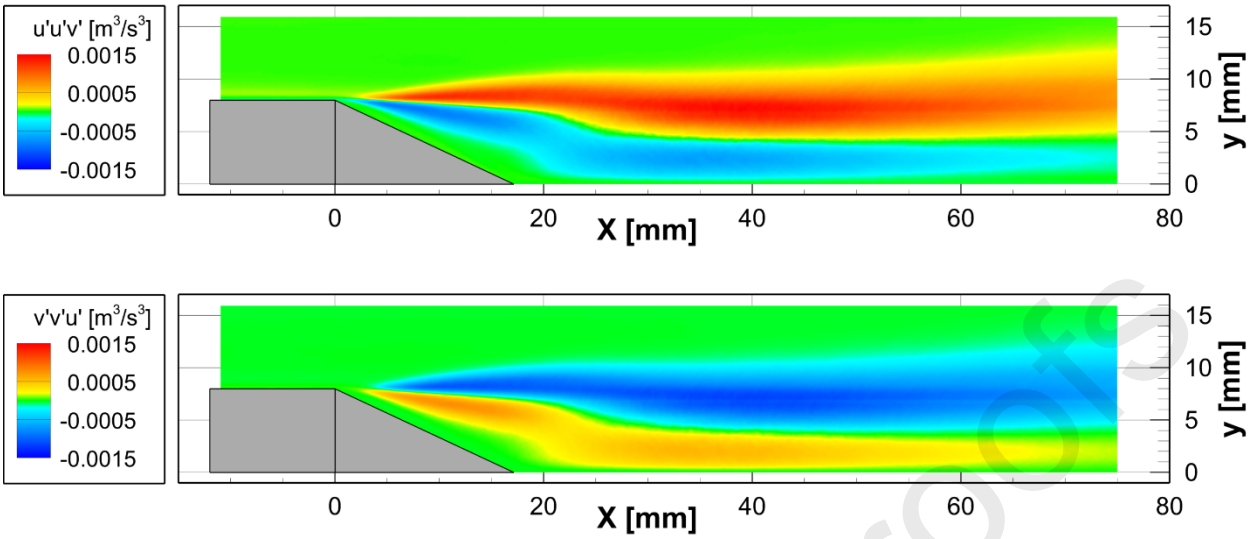

Figure 22: time- and spanwise-averaged distributions of selected triple-correlations: *u'u'v'* (top) and *v'v'u'* (bottom).

References

[1] Simpson RL (1985) Two-dimensional turbulent separated flow. *AGARDograph* AG 287, Vol. 1.

[2] Simpson RL (1989) Turbulent boundary-layer separation. *Annual Review of Fluid Mechanics* AG 21: 205–234.

[3] Bak C (2022) Airfoil Design. In: Stoevesandt B, Schepers G, Fuglsang P, Sun Y (eds.) *Handbook of Wind Energy Aerodynamics*, Springer Nature, Cham, Switzerland. Chap. 4.

[4] Spalart PR, Venkatakrishnan V (2016) On the role and challenges of CFD in the aerospace industry. *The Aeronautical Journal* 120(1223): 209–232.

[5] Eaton JK, Johnston JP (1981) A Review of Research on Subsonic Turbulent Flow Reattachment. *AIAA Journal* 19(9): 1093–1100.

[6] Chen L, Asai K, Nonomura T, Xi G, Liu T (2018) A review of Backward-Facing Step (BFS) flow mechanisms, heat transfer and control. *Thermal Science and Engineering Progress* 6: 194–216.

[7] Borgmann D, Cura C, Weiss J, Little J (2024) Three-Dimensional Nature of Low-Frequency Unsteadiness in a Turbulent Separation Bubble. *AIAA Journal* 62(11): 4349–4363.

[8] Gray P, Gluzman I, Thomas F, Corke TC (2026) Smooth-body flow separation over a tapered Gaussian bump – flow field topography and topology. *Journal of Fluid Mechanics* 1032: A54.

[9] Ma X, Schröder A (2017) Analysis of flapping motion of reattaching shear layer behind a two-dimensional backward-facing step. *Physics of Fluids* 29: 115104.

Journal Pre-proofs

[10] Mohammed-Taifour A, Weiss J (2021) Periodic forcing of a large turbulent separation bubble. *Journal of Fluid Mechanics* 915: A24.

[11] Le Floc'h A, Weiss J, Mohammed-Taifour A, Dufresne L (2020) Measurements of pressure and velocity fluctuations in a family of turbulent separation bubbles. *Journal of Fluid Mechanics* 902: A13.

[12] Kuehn (1980) Effects of Adverse Pressure Gradient on the Incompressible Reattaching Flow over a Rearward-Facing Step. *AIAA Journal* 18(3): 343–344.

[13] Armaly BF, Durst F, Pereira JCF, Schönung B (1983) Experimental and theoretical investigation of backward-facing step. *Journal of Fluid Mechanics* 127: 473–496.

[14] Driver DM, Seegmiller HL (1985) Features of a Reattaching Turbulent Shear Layer in Divergent Channel Flow. *AIAA Journal* 23(2): 163–171.

[15] Le H, Moin P, Kim J (1997) Direct numerical simulation of turbulent flow over a backward-facing step. *Journal of Fluid Mechanics* 330: 349–374.

[16] Kostas J, Soria J, Chong MS (2002) Particle image velocimetry measurements of a backward-facing step flow. *Experiments in Fluids* 33(6): 838–853.

[17] Ma X, Tang Z, Jiang N (2022) Investigation of spanwise coherent structures in turbulent backward-facing step flow by time-resolved PIV. *Experimental Thermal and Fluid Science* 132: 110569.

[18] Zheng K, Setiawan H, Philip J, Lee J, Monty JP (2024) Flows over backward-facing steps with different spanwise widths. *Physical Review Fluids* 9: 124601.

[19] Ruck B, Makiola B (1993) Flow separation over the step with inclined walls. In: So RMC, Speziale CG, Launder BE (eds.) *Near-Wall Turbulent Flows*, Elsevier, Amsterdam, pp. 999–1008.

[20] Ahn JW, Park TS, Sung HJ (1997) Application of a near-wall turbulence model to the flows over a step with inclined wall. *International Journal of Heat and Fluid Flow* 18: 209–217.

[21] Guilmineau E, Duvigneau R, Labroquère J (2014) Optimization of jet parameters to control the flow on a ramp. *Comptes Rendus Mecanique* 342: 363–375.

[22] Joseph P, Bortolus D, Grasso F (2014) Flow control on a 3D backward facing ramp by pulsed jets. *Comptes Rendus Mecanique* 342: 376–381.

[23] Kourta A, Thacker A, Joussot R (2015) Analysis and characterization of ramp flow separation. *Experiments in Fluids* 56: 104.

[24] Stella F, Mazellier N, Kourta A (2017) Scaling of separated shear layers: an investigation of mass entrainment. *Journal of Fluid Mechanics* 826: 851–887.

[25] Hlevca D, Gilliéron P, Grasso F (2018) Experimental study of the active control applied to the flow past a backward facing ramp. *Experiments in Fluids* 59: 39.

[26] Weiss J, Steinfurth B, Chamard L, Giani A, Combette P (2022) Spectral proper orthogonal decomposition of unsteady wall shear stress under a turbulent separation bubble. *AIAA Journal* 60(4): 2150–2159.

[27] Gilotte P, Mortazavi I, Edwige S (2024) Active control and modal decomposition for the flow over a ramp. *International Journal of Heat and Fluid Flow* 107: 109374.

[28] Steinfurth B, Weiss J (2024) Assimilating experimental data of a mean three-dimensional separated flow using physics-informed neural networks. *Physics of Fluids* 36: 015131.

[29] Tandon S, Maki KJ, Johnsen E (2024) Large-Eddy Simulations of Flow over a Backward-Facing Ramp with a Wall-Mounted Cube. *AIAA Journal* 62(9): 3403–3417.

[30] Rohlfs L, Weiss J (2025) SENSE—Sensor-Enhanced Neural Shear stress Estimation for quantitative oil-film visualizations. *Experiments in Fluids* 66: 187.

[31] Greenblatt D, Paschal KB, Yao CS, Harris J, Schaeffler NW, Washburn AE (2006) Experimental investigation of separation control part 1: baseline and steady suction. *AIAA Journal* 44(12): 2820–2830.

[32] Borra A, Saxton-Fox T (2024) Comparison of a turbulent boundary layer encountering a ramp versus a bump. *Proceedings 13th International Symposium on Turbulence and Shear Flow Phenomena (TSFP13)*, Montreal, Canada.

[33] Duetsch-Patel JE, MacGregor D, Jenssen YL, Henry PY, Muthanna C, Savio L, Lavoie P, Gargiulo A, Sundarraj V, Ozoroski TA, Roy CJ, Devenport WJ, Borgoltz A, Lowe T (2022) The BeVERLI Hill three-dimensional separating flow case: cross-facility comparisons of validation experiment results. *AIAA Paper* 2022-0698.

[34] Deck S (2012) Recent improvements in the Zonal Detached Eddy Simulation (ZDES) formulation. *Theoretical and Computational Fluid Dynamics* 26: 523–550.

[35] NASA (2018) *NASA's 40% Challenge and CFD Prediction Error Assessment Workshop*. https://turbmodels.larc.nasa.gov/nasa40percent.html. [Retrieved 09 10 2025]

[36] Song S, David B. DeGraaff DB, Eaton JK (2000) Experimental study of a separating, reattaching, and redeveloping flow over a smoothly contoured ramp. *International Journal of Heat and Fluid Flow* 21: 512–519.

[37] Debien A, von Krbek KAFF, Mazellier N, Duriez T, Cordier L, Noack BR, Abel MW, Kourta A (2016) Closed-loop separation control over a sharp edge ramp using genetic programming. *Experiments in Fluids* 57: 40.

[38] Simmons DJ, Thomas FO, Corke TC, Gluzman I (2024) Experimental characterization and similarity scaling of smooth-body flow separation and reattachment on a two-dimensional ramp geometry. *Journal of Fluid Mechanics* 1000: A12.

[39] Steinfurth B, Li M, Scarano F, Weiss J (2025) Three-dimensional low-frequency dynamics of a turbulent separation bubble. *Journal of Fluid Mechanics* 1019: R4.

[40] Chen L, Kawase C, Nonomura T, Asai K (2020) Dynamic surface heat transfer and re- attachment flow measurement using luminescent molecular sensors. *International Journal of Heat and Mass Transfer* 155: 119684.

[41] Schröder A, Schanz D (2023) 3D Lagrangian particle tracking in fluid mechanics. *Annual Review of Fluid Mechanics* 55: 511-540.

[42] Schanz D, Gesemann S, Schröder A (2016) Shake-The-Box: Lagrangian particle tracking at high particle image densities. *Experiments in Fluids* 57: 70.

[43] Novara M, Schanz D, Geisler R, Gesemann S, Voss C, Schröder A (2019) Multi-exposed recordings for 3D Lagrangian particle tracking with Multi-Pulse Shake-The-Box. *Experiments in Fluids* 60: 44.

[44] Jahn T, Schanz D, Schröder A (2021) Advanced iterative particle reconstruction for Lagrangian particle tracking. *Experiments in Fluids* 62: 179.

[45] Schanz D, Novara M, Schröder A (2021) Shake-The-Box particle tracking with variable time-steps in flows with high velocity range (VT-STB). *Proceedings of the 14th International Symposium on Particle Image Velocimetry*, virtual event.

[46] Schanz D, Schröder A, Bosbach J, Strübing T, Wolf C, Schwarz C, Heintz A (2024) Scanning Lagrangian particle tracking to measure 3D large scale aerodynamics of quadcopter flight. *Proceedings of the 21st International Symposium on Applications of Laser and Imaging Techniques to Fluid Mechanics*, Lisbon, Portugal.

[47] Liu T, Sullivan JP, Asai K, Klein C, Egami Y (2021) *Pressure- and Temperature-Sensitive Paints*. 2nd ed., Springer Nature, Cham, Switzerland.

[48] Miozzi M, Capone A, Costantini M, Fratto L, Klein C, Di Felice F (2019) Skin friction and coherent structures within a laminar separation bubble. *Experiments in Fluids* 60: 13.

[49] Miozzi M, Di Felice F, Klein C, Costantini M (2020) Taylor hypothesis applied to direct measurement of skin friction using data from Temperature Sensitive Paint. *Experimental Thermal and Fluid Science* 110: 109913.

[50] Costantini M, Henne U, Klein C, Miozzi M (2021b) Skin-Friction-Based Identification of the Critical Lines in a Transonic, High Reynolds Number Flow via Temperature-Sensitive Paint. *Sensors* 21(15): 5106.

[51] Miozzi M, Costantini M (2021) Temperature and skin-friction maps on a lifting hydrofoil in a propeller wake. *Measurement Science and Technology* 32: 114007.

[52] Miozzi M, Schröder A, Schanz D, Willlert CE, Klein C, Lemarechal J (2024) Skin-friction from temperature and velocity data around a wall-mounted cube. *Experiments in Fluids* 65: 156.

[53] Grabe C (2022) DLR-Project ADaMant: Adaptive, Data-driven Physical Modeling towards Border of Envelope Applications. *Proceedings DLRK 2022*, Dresden, Germany.

[54] Dandois J, Garnier E, Sagaut P (2007) Numerical simulation of active separation control by a synthetic jet. *Journal of Fluid Mechanics* 574: 25–58.

[55] Chiatto M, de Luca L, Grasso F (2021) Modal analysis of actively controlled flow past a backward facing ramp. *Physical Review Fluids* 6: 064608.

[56] Costantini M, Schanz D, Geisler R, Schröder A, Knopp T, Dormoy C, Grabe C, Miozzi M (2023) Experimental and numerical study of geometry-induced separation of a turbulent boundary layer. *Proceedings DLRK 2023*, Stuttgart, Germany.

[57] Guerin M, Knopp T, Grabe C, Costantini M, Schröder A, Schanz D, Geisler R (2026) Experimental Data Analysis of Mean Flow and Turbulence over a Backward Facing Step for RANS Turbulence Modeling. In: Dillmann A, Heller G, Krämer E, Breitsamter C, Wagner C, Krenkel L (eds.) *New Results in Numerical and Experimental Fluid Mechanics XV*, Notes on Numerical Fluid Mechanics and Multidisciplinary Design 156, Springer Nature, Cham, 2026.

[58] Scholz P, Sattler S, Wulff D (2013) Der Große Wasserkanal "GWB" – Eine Versuchsanlage für zeitauflösende Messungen bei großen Reynoldszahlen. *Proceedings DLRK 2013*, Stuttgart, Germany.

[59] Eisfeld B (2022) The importance of turbulent equilibrium for Reynolds-stress modeling. *Physics of Fluids* 34: 025123.

[60] Foroozan F, Ianiro A, Discetti S, Baars WJ (2025) Resolving convective velocities of turbulent boundary layer-induced convective heat transfer fluctuations at the wall. *Physical Review Fluids* 10: 094904.

[61] Schülein E, Reuther N, Knopp T (2018) Optical skin friction measurements in a turbulent boundary layer with pressure gradient. In: Dillmann A, Heller G, Krämer E, Wagner C, Bansmer S, Radespiel R, Semaan R (eds.) *New Results in Numerical and Experimental Fluid Mechanics XI*, Notes on Numerical Fluid Mechanics and Multidisciplinary Design 136, Springer International Publishing, Cham, Switzerland, pp. 95–104.

[62] Fey U, Klein C, Möller TJ, Pöttner J, Radespiel R, Ondrus V, Beifuss U (2013) Investigation of Circular Cylinder Flow in Water Using Temperature-Sensitive Paint. In: Dillmann A, Heller G, Kreplin HP, Nitsche W, Peltzer I (eds.) *New Results in Numerical and Experimental Fluid Mechanics VIII*, Notes on Numerical Fluid Mechanics and Multidisciplinary Design 121, Springer-Verlag, Berlin Heidelberg, pp. 657–664.

[63] Capone A, Klein C, Di Felice F, Beifuss U, Miozzi M (2015) Fast-response underwater TSP investigation of subcritical instabilities of a cylinder in crossflow. *Experiments in Fluids* 56: 196.

[64] Miozzi M, Capone A, Di Felice F, Klein C, Liu T (2016) Global and local skin friction diagnostics from TSP surface patterns on an underwater cylinder in crossflow. *Physics of Fluids* 28: 124101.

[65] Lemarechal J, Klein C, Henne U, Puckert DK, Rist U (2019) Detection of Lambda- and Omega-vortices with the temperature-sensitive paint method in the late stage of controlled laminar–turbulent transition. *Experiments in Fluids* 60: 91.

[66] Lemarechal J, Klein C, Puckert DK, Rist U (2021) Application of the temperature-sensitive paint method for quantitative measurements in water. *Measurement Science and Technology* 32: 105301.

[67] Miozzi M, Capone A, Klein C, Costantini M (2021). Incipient stall characterization from skin- friction maps. *International Journal of Numerical Methods for Heat & Fluid Flow* 31: 674–693.

[68] Venenciuc TV, Klein C, Yarusevych S, Hain R, Kähler CJ (2024) Laminar separation bubble analysis by means of single-shot lifetime temperature sensitive paint in a water towing tank. *Measurement Science and Technology* 35: 075301.

[69] Costantini M, Dimond BD, Klein C, Sattler S, Miozzi M (2026a) Transitional Phenomena on an Elliptic Profile. In: Kato K, Inasawa A, Matsubara M (eds.) *Proceedings of the 10th IUTAM Symposium on Laminar-Turbulent Transition*, IUTAM Bookseries 44, Springer Nature, Singapore, pp. 271–278.

[70] Lin N, Reed HL, Saric WS (1992) Effect of Leading Edge Geometry on Boundary-Layer Receptivity to Freestream Sound. In: Hussaini M, Kumar A, Streett C (eds.) *Instability, Transition and Turbulence*, Springer-Verlag, New York, pp. 421–440.

[71] Fey U, Egami E (2007). Transition-Detection by Temperature-Sensitive Paint. In: Tropea C, Yarin AL, Foss JF (eds.) *Springer Handbook of Experimental Fluid Mechanics*. Springer-Verlag, Berlin Heidelberg. Chap. 7.4.

[72] Asai K, Kanda H, Kunimasu T, Liu T, Sullivan JP (1997) Boundary-Layer Transition Detection in a Cryogenic Wind Tunnel Using Luminescent Paint. *Journal of Aircraft* 34(1): 34–42.

[73] Egami Y, Fey U, Klein C, Sitzmann M, Wild J (2006) Transition Detection on High-Lift Devices in DNW-KKK by means of Temperature-Sensitive Paint. In: Grant I (ed.) *12th International Symposium on Flow Visualization*, Optimage Ltd., Edinburgh, UK. Paper No. 237.

[74] Egami Y, Klein C, Henne U, Bruse M, Ondrus V, Beifuss U (2009) Development of a Highly Sensitive Temperature-Sensitive Paint for Measurements under Ambient (0 – 60 °C) Conditions. *AIAA Paper* 2009-1075.

[75] Klein C, Henne U, Sachs WE, Beifuss U, Ondrus V, Bruse M, Lesjak R, Löhr M, Becher A, Zhai J (2015) Combination of Temperature-Sensitive Paint (TSP) and Carbon Nanotubes (CNT) for Transition Detection. *AIAA Paper* 2015-1558.

[76] Costantini M, Hein S, Henne U, Klein C, Koch S, Schojda L, Ondrus V, Schröder W (2016) Pressure Gradient and Non-adiabatic Surface Effects on Boundary-Layer Transition. *AIAA Journal* 54(11): 3465–3480.

[77] Weiss A, Gardner AD, Klein C, Raffel M (2017) Boundary-layer transition measurements on Mach-scaled helicopter rotor blades in climb. *CEAS Aeronautical Journal* 8(4): 613–623.

[78] Klein C, Yorita D, Henne U, Ondrus V, Hensch AK, Longo R, Gimbel A, van Deetzen S (2020) Application of Temperature Sensitive Paint to Investigate Laminar-to-Turbulent Transition on Nacelles. *AIAA Paper* 2020-1608.

[79] Costantini M, Henne U, Risius S, Klein, C (2021a) A robust method for reliable transition detection in temperature-sensitive paint data. *Aerospace Science and Technology* 113: 106702.

[80] Costantini M, Fuchs C, Henne U, Klein C, Ondrus V, Bruse M, Löhr M, Jacobs M (2021c) Experimental Analysis of the Performance of a Wind-Turbine Airfoil Using Temperature-Sensitive Paint. *AIAA Journal* 59(11): 4449–4464.

[81] Ondrus V, Meier R, Klein C, Henne U, Schäferling M, Beifuss U (2015) Europium 1,3-di(thienyl)propane-1,3-diones with Outstanding Properties for Temperature Sensing. *Sensors and Actuators A: Physical* 233: 434–441.

[82] Arkema (2025) ORGASOL® 2002 D NAT 1 Ultrafine polyamide powder. https://hpp.arkema.com/en/products/product/f/spa_hpp_Orgasol/p/orgasol-2002-d-nat-1/ [Retrieved 09 10 2025]

[83] Glasfaser-Flugzeug-Service GmbH Hansjörg Streifeneder (2024) 3D Turbulator tape 60°/0.205 mm, 6 mm between teeth. https://streifly.de/en/home/tapes/ [Retrieved 28 02 2024]

[84] Dimond BD (2024) Investigation of boundary layer transition at high Reynolds numbers using time-resolved temperature-sensitive paint. *PhD thesis*, Georg-August-Universität Göttingen.

[85] Eckelmann H (1974). The structure of the viscous sublayer and the adjacent wall region in a turbulent channel flow. *Journal of Fluid Mechanics* 65: 439–459.

[86] Kim J, Hussain F (1993). Propagation velocity of perturbations in turbulent channel flow. *Physics of Fluids* A 5: 695–706.

[87] Hetsroni G, Tiselj I, Bergant R, Mosyak A, Pogrebnyak E (2004) Convection velocity of temperature fluctuations in a turbulent flume. *Journal of Heat Transfer* 126: 843–848.

[88] Liu T, Chen T, Miozzi M (2024) Correlation between skin friction and enstrophy convection velocity in near-wall turbulence. *European Journal of Mechanics - B/Fluids* 104: 224-230.

[89] Del Álamo JC, Jimenéz, J (2009) Estimation of turbulent convection velocities and corrections to Taylor's approximation. *Journal of Fluid Mechanics* 640: 5–26.

[90] Geng C, He G, Wang Y, Xu C, Lozano-Duran A, Wallace JM (2015) Taylor's hypothesis in turbulent channel flow considered using a transport equation analysis. *Physics of Fluids* 27: 025111.

[91] Taylor GI (1938) The spectrum of turbulence. *Proceedings of the Royal Society of London. Series A - Mathematical and Physical Sciences* 164: 476–490.

[92] Schanz D, Geisler, R, Lemarechal J, De Vincenzo A, Knopp T, Schröder A (2025) Volumetric investigation of geometry-induced separation of a turbulent boundary layer. *Proceedings of the 16th International Symposium on Particle Image Velocimetry – ISPIV 2025*, Tokyo, Japan.

[93] Gesemann S, Huhn F, Schanz D, Schröder A (2016) From noisy particle tracks to velocity, acceleration and pressure fields using B-splines and penalties. *Proceedings of the 18th International Symposium on Applications of Laser and Imaging Techniques to Fluid Mechanics,* Lisbon, Portugal.

[94] Schröder A, Schanz D, Michaelis D, Cierpka C, Scharnowski S, Kähler CJ (2015) Advances of PIV and 4D-PTV "Shake-The-Box" for Turbulent Flow Analysis –the Flow over Periodic Hills. *Flow Turbulence and Combustion* 95: 193–209.

[95] Godbersen P, Gesemann S, Schanz D, Schröder A (2024) FlowFit3: Efficient data assimilation of LPT measurements. *Proceedings of the 21th International Symposium on the Application of Laser and Imaging Techniques to Fluid Mechanics,* Lisbon, Portugal.

[96] Delery JM (2013) *Three-dimensional separated flows topology*. Wiley, Hoboken, USA.

[97] Mäteling E, Lemarechal J, Klein C, Puckert DK, Rist U (2020) Experimental investigation of mixed convection in horizontal channel flow in combination with cylindrical roughness elements. In: Dillmann A, Heller G, Krämer E, Wagner C, Tropea C, Jakirlić S (eds.) *New Results in Numerical and Experimental Fluid Mechanics XII*, Notes on Numerical Fluid Mechanics and Multidisciplinary Design 142, Springer International Publishing, Cham, Switzerland, pp. 533–542.

[98] Marusic I, McKeon BJ, Monkewitz PA, Nagib HM, Smits AJ, Sreenivasan KR (2010) Wall-bounded turbulent flows at high Reynolds numbers: Recent advances and key issues. *Physics of Fluids* 22: 065103.

[99] Bross M, Schanz D, Novara M, Eich F, Schröder A, Kähler CJ (2023) Turbulent superstructure statistics in a turbulent boundary layer with pressure gradients. *European Journal of Mechanics / B Fluids* 101: 209–218.

[100] Khintchine A (1934) Korrelationstheorie der stationären stochastischen Prozesse. *Mathematische Annalen* 109: 604–615.

Journal Pre-proofs

Journal Pre-proofs

Submitted to the Special Issue of *Experimental Thermal and Fluid Science* (*ETFS*) dedicated to the 6th International Conference on Experimental Fluid Mechanics (ICEFM). Revision R1

Declaration of interests

☒ The authors declare that they have no known competing financial interests or personal relationships that could have appeared to influence the work reported in this paper.

☐ The authors declare the following financial interests/personal relationships which may be considered as potential competing interests:

Journal Pre-proofs

Journal Pre-proofs

Submitted to the Special Issue of *Experimental Thermal and Fluid Science* (*ETFS*) dedicated to the 6th International Conference on Experimental Fluid Mechanics (ICEFM). Revision R1

Study of Ramp-Induced Turbulent Boundary Layer Separation and Reattachment via Temperature-Sensitive Paint and Lagrangian Particle Tracking

Marco Costantini[1], Christian Klein[1], Andrea De Vincenzo[1,2], Reinhard Geisler[1], Philipp Godbersen[1], Jonathan Lemarechal[1], Daniel Schanz[1], Andreas Schröder[1,3], Tobias Knopp[1], Cornelia Grabe[1], Stephan Sattler[4], Massimo Miozzi[5]*

[1] DLR, Institute of Aerodynamics and Flow Technology, Göttingen, Germany

[2] Politecnico di Milano, School of Industrial and Information Engineering, Milan, Italy

[3] Brandenburg TU, Chair of Image Based Measurement Techniques, Cottbus, Germany

[4] TU Braunschweig, Institute of Fluid Mechanics, Braunschweig, Germany

[5] CNR, Institute of Marine Engineering, Rome, Italy

*Marco.Costantini@dlr.de

Highlights

- Time- and space-resolved three-dimensional flowfield and surface temperature maps
- Distributions of velocity, acceleration, Reynolds stresses and triple correlations
- Map of celerity of propagation of temperature fluctuations at the wall
- Agreement of time-averaged reattachment location from velocity and celerity fields
- Quantified spanwise arrangement of flowfield structures and wall thermal traces

Journal Pre-proofs